

Fachbereich Mathematik und Naturwissenschaften Fachgruppe Physik Bergische Universität Wuppertal

Performance studies of b-tagging algorithms for single top-quark analyses with the ATLAS detector at $\sqrt{s}=7$ TeV

Master Thesis
von
Phillipp Tepel

14. September 2012

Contents

1	Introduction	1
2		3 4 6 7
3	3.1 The Large Hadron Collider	13 16 18 18 21 22 24
4	4.1 Monte Carlo Simulation	27 28 30 31 34
5	Comparison of AcerMC and POWHEG MC Generators	35 36 40 41 43 45
6	0	47 47

	6.2	Vertex Reconstruction	48
	6.3	Charged Lepton Identification	48
	6.4	Jet Reconstruction	49
	6.5	Missing Transverse Momentum	50
7	b-ta	gging	51
	7.1	Baseline Track Selection	52
	7.2	b-tagging Algorithms	52
		7.2.1 Impact parameter tagging algorithms	52
		7.2.2 Secondary vertex tagging algorithms	54
		7.2.3 Combining tagging algorithms	54
		7.2.4 $\operatorname{JetFitterCOMBNN}(c)$	54
		7.2.5 MV1	55
	7.3	Studies on b -tagging Calibration	57
8	b-ta	gging Algorithms for Single Top-Quark Analyses	65
	8.1	Event Selection and Signature	65
	8.2	Comparison of b -tagging Algorithms in Single Top-Quark Analyses	69
	8.3	b-tagging Optimisation	73
	8.4	Evaluation of Systematic Uncertainties	78
9	Cor	aclusion	81
Li	${f st}$ of	Figures	83
Li	${f st}$ of	Tables	85
${f B}$ i	ibliog	graphy	86

1 Introduction

The ambition of particle physics is understanding the fundamental building blocks of matter and their interactions. Since the early 20th century, experiments have been conducted, devoted to study the structure of matter. Theories have been spawned that lead to the formulation of the Standard Model of particle physics in the mid 1970s. Since then, the theory that is the Standard Model, had to endure a series of experimental and theoretical tests and has been further developed in the process. Even though, the Standard Model describes most of the fundamental particles and their interaction, it does not yet incorporate gravity. The key to investigate the elementary substructure of atoms are collision experiments. The resolution capability of collision experiments of that type depends on the energy of the colliding particles. In addition, the only possibility to create massive particles, is to provide the required energy.

The Large Hadron Collider (LHC) is the most powerful particle accelerator created so far. Four major experiments are located at the LHC. The studies presented in this thesis are using the 2011 collision data, recorded by ATLAS, in which the LHC was operated at $\sqrt{s} = 7$ TeV center-of-mass collision energy.

As of today, six different quarks are known to exist. The by far heaviest of them is the top quark, with a mass of $m_t = 173.2 \pm 0.9$ GeV [1]. It has been discovered in 1995 at the Tevatron collider by the CDF and DZero experiments [2, 3]. The top-quark mass is of the same order as the electroweak symmetry breaking scale, and top quarks are therefore well suited for precision tests of the Standard Model at this scale. At hadron colliders the top-quark pair-production process via the strong interaction is the most dominant one, while single top quarks can be produced via the electroweak interaction. Single top-quark events are composed of three different production channels that can be differentiated. The t- and s-channel production modes are both involving a virtual W boson exchange, whereas the associated production of a top quark involves a real W boson. At the LHC, the t-channel production mode of single top-quarks is the dominant one.

In order to understand the modeling of the single top-quark t-channel events provided by MC generators kinematic properties of the single top-quark t-channel are studied in the first part of this thesis. The kinematic properties of final state particles of the single top-quark t-channel are compared for MC event generators and next-to-leading-order calculation.

1 Introduction

In the Standard Model, a top-quark decays into a W boson and a b quark with a branching ratio of nearly 100%, therefore the identification capability of a b-quark jet is crucial for most physics processes involving top quarks. The so called b-tagging, is used to efficiently reduce high cross-section background which is not involving the production of a b-quark. As a result, the performance of single top-quark analyses depends on the understanding of b-tagging. Different b-tagging algorithms are available exploiting the characteristics of the jet containing a b-quark. Most b-tagging algorithms need to be calibrated, to account for modeling differences between simulated events and collision data. These calibrations are performed for defined working points corresponding to a tagging efficiency, and provide scaling factors. Within this thesis, a b-tagging calibration is studied which yields a continuous scaling function instead of discrete values. To perform the calibration a sample of simulated dijet events is used, which is enriched in b-quark jet events, using a "tag and probe" method.

In the scope of this thesis different tagging algorithms are compared in terms of their impact on the performance of single top-quark analyses and the impact of the associated systematic uncertainties. The performance is evaluated using the ratio of signal and background events (S/B). Two approaches are presented to combine b-taggers and the respective performance is investigated.

2 The Standard Model of Particle Physics

The standard model of particle physics (SM), is meant to describe all fundamental particles and the interactions between them. Particles are subdivided into two classes, particles with half-integer spin $s = \left\{\frac{1}{2}, \frac{3}{2}, \ldots\right\}$ are called fermions, while particles with integer spin $s = \{0, 1, \ldots\}$ are called bosons, however only particles with $s = \left\{0, 1, \frac{1}{2}\right\}$ are included in the SM.

The fundamental interactions are described by the electromagnetic- strong- and weak force. Gravitation is the fourth fundamental interaction which is described by general relativity and not included in the SM. Over the last decades, plenty of measurements in the field of elementary particle physics has been conducted and they are, as of today, all in agreement with the SM predictions.

2.1 Matter and Particles

All fermions are described by the Fermi-Dirac statistic [4] and must therefore obey the Pauli exclusion principle. The Pauli exclusion principle states, that no two identical fermions can have identical sets of quantum numbers.

Every matter particle in the Standard Model is either a quark or a lepton. Quarks can be of type up- or down-, whereas leptons are grouped by their electric charge. All fermions are subdivided into three generations (cf. Table 2.1). All atoms are composed of first-generation fermions. The remaining two generations of fermions can only be produced in high-energy reactions. The emerging fermions decay almost immediately into fermions of the first generation. All fundamental particles and anti-particles are subject to fundamental interactions which are discussed in further detail below.

Table 2.1: Fermions of the Standard Model, subdivided into quarks and leptons. Particles of the second and third generation have higher mass than those of the first generation, but are otherwise identical.

Type	El. charge $[e]$	1. generation	2. generation	3. generation
Quarks	2/3 - 1/3		$ \begin{array}{c} \text{charm } (c) \\ \text{strange } (s) \end{array} $	$ top (t) \\ bottom (b) $
Lepton Neutrino	-1 0	electron (e) ν_e	muon (μ) ν_{μ}	

2.2 Interactions and Gauge Bosons

Each force is mediated by a vector boson, summarised in Table 2.2, except gravity, since it is not described by the SM. In particle physics the impact of gravitation is negligible, due to the huge difference in strength which is more than 30 orders of magnitude compared to the weak force. In which interaction a particle participates, depends on the charge it carries. A particle can have electromagnetic, strong and or weak charge, whereas gravitation only affects particles with mass.

Table 2.2: Vector Bosons of the Standard Model.

Interaction	Boson	El. charge $[e]$	Spin	Mass [GeV]
Electromagnetic	Photon	0	1	0
XX 7 1	W^{\pm}	± 1	1	80.4
Weak	Z	0	1	91.2
Strong	Gluon	0	1	0

The theory of the strong interaction is called quantum chromodynamics (QCD). QCD describes the interaction of particles and anti-particles which carry colour charge. The colour charge, unlike the electromagnetic charge, can have three states namely blue, green and red, as well as their anti-colours. Quarks are the only fermions which carry colour charge and are therefore subject to QCD. At the present energy scale of the Universe, nature does not allow stable coloured particles, thus quarks can only be observed in compound objects. The colour confinement prevents the observation of singular quarks. Quarks group either into mesons, which consist of one quark and one anti-quark, or baryons which contain three quarks. Both compound objects do not have colour charge. These compound objects are called hadrons in general.

Quantum Electrodynamics (QED) [5] is describing the electromagnetic interaction using quantum mechanics and special relativity. Every particle which carries an electrical charge is subject to the electromagnetic interaction, which is mediated by a photon.

The weak interaction effects all fermions. It is mediated via the W^{\pm} and Z^0 bosons, which have substantial mass, thus rendering the weak force short ranged. The weak isospin (T_3) is a quantum number of all particles. The isospin steers the interaction of particles with the weak force. One key attribute of the weak force is that its charged bosons couples only to left-handed particles and right-handed antiparticles.

When interacting with the weak force a quark will change its flavour. This flavour change cannot occur within the same quark family, but across families. The Cabibbo-Kobayashi-Maskawa (CKM) matrix connects the mass (d, s, b) eigenstates of a quark to the corresponding mixture of weak eigenstates (d', s', b') (cf. equation 2.1).

$$\begin{pmatrix} d' \\ s' \\ b' \end{pmatrix} = \begin{pmatrix} V_{ud} & V_{us} & V_{ub} \\ V_{cd} & V_{cs} & V_{cb} \\ V_{td} & V_{ts} & V_{tb} \end{pmatrix} \begin{pmatrix} d \\ s \\ b \end{pmatrix}$$
(2.1)

The product of the weak coupling constant and the CKM-matrix element V_{ij} yields the coupling of the quarks (i, j) and the W boson. The values of the CKM-matrix-elements are not predicted by the SM, but have to be obtained from experiment [6]:

$$V = \begin{pmatrix} 0.97427^{+0.00015}_{-0.00015} & 0.22534^{+0.00065}_{-0.00065} & 0.00351^{+0.00015}_{-0.00014} \\ 0.22520^{+0.00065}_{-0.00065} & 0.97344^{0.00016}_{-0.00016} & 0.0412^{+0.0011}_{-0.0005} \\ 0.00867^{+0.00029}_{-0.00031} & 0.0404^{+0.0011}_{-0.0005} & 0.999146^{+0.000021}_{-0.000046} \end{pmatrix}.$$
(2.2)

Weak interaction decay processes can occur in three different forms. Leptonic decays, for one, are those which only involve leptons. The second group are the semi-leptonic decays, which involve both hadrons and leptons, e.g. the nuclear beta-decay. The third category are fully hadronic decay modes. The theory of quantum electrodynamics and the weak interaction has been combined into an unified electroweak theory. It was achieved by Glashow, Weinberg and Salam [7]. It states that at high energies both forces will merge.

Physical processes between particles can be visualised and computed with Feynman diagrams. A Feynman diagram represents the quantum mechanical matrix element of particular transition process, for example a decay or a scattering process. Calculations of different aspects of a process can be achieved by casting all associated diagrams via the Feynman rules. In Figure 2.1 an example of a Feynman diagram of an electron and positron annihilation is depicted.

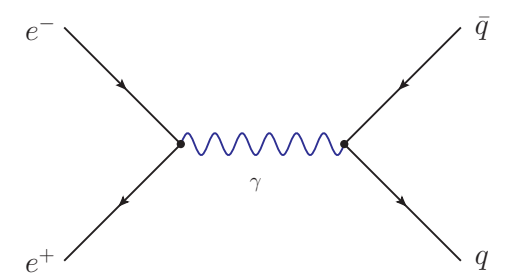


Figure 2.1: In this Feynman diagram, an electron and a positron annihilate, producing a photon (represented by the blue wave). From that photon a quark-antiquark pair emerges.

2.3 Top Quark Production and Decay

The top quark is the heaviest of all known quarks, thus the production requires an enormous amount of collision energy, which could not be reached until the Tevatron collider was constructed. In 1995 top quark has been discovered by the CDF and DZero experiments at the Tevatron collider [2, 3]. Latest results of top-quark mass combination yields $m_t = 173.2 \pm 0.9$ GeV [1]. The top quark, like all quarks, can be produced via the strong or the weak force. The major production mode for top quarks at the LHC is the gluon-gluon fusion channel, with a top quark-antiquark pair in the final state (cf. Figure 2.2). Due to its high mass, the average lifetime of the top quark is extremely short, with $\tau_t \approx 5 \cdot 10^{-25}$ s [8]. This implicates, that the top quark will not hadronise before it decays, since the lifetime is smaller than the hadronisation time scale, thus the top quark can be observed as a quasi-free particle. This is a remarkable feature of the top-quark decay, compared to other quarks, which enables the possibility to investigate certain attributes (e.g. spin properties).

The top-quark decays almost exclusively weakly into a W boson and a b quark, due to the fact that the CKM-matrix element V_{tb} (cf. Equation 2.2) is close to unity.

The production of top quarks can also occur, although less likely, via the weak force. The importance of single top-quark production arises from probing the electroweak theory. Furthermore, it is key in the search for new physics since the top-quark mass is of the same order of magnitude as the electroweak symmetry breaking scale.

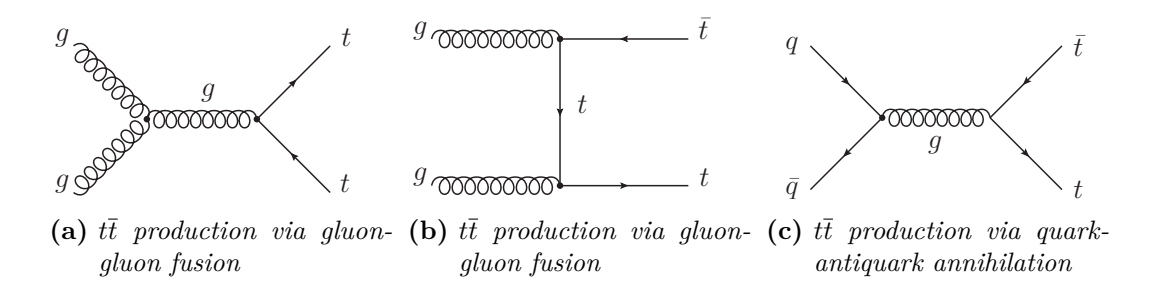


Figure 2.2: Dominant leading-order top-quark pair production modes at the LHC.

2.3.1 Single Top-Quark production

Figure 2.3(a) shows the dominating production mode of single top-quarks which is the t-channel, that proceeds via the exchange of a space-like W boson. The s-channel 2.3(b), which proceeds via an exchange of a time-like W boson and the associated production, called Wt production, 2.3(c) are relevant as well.

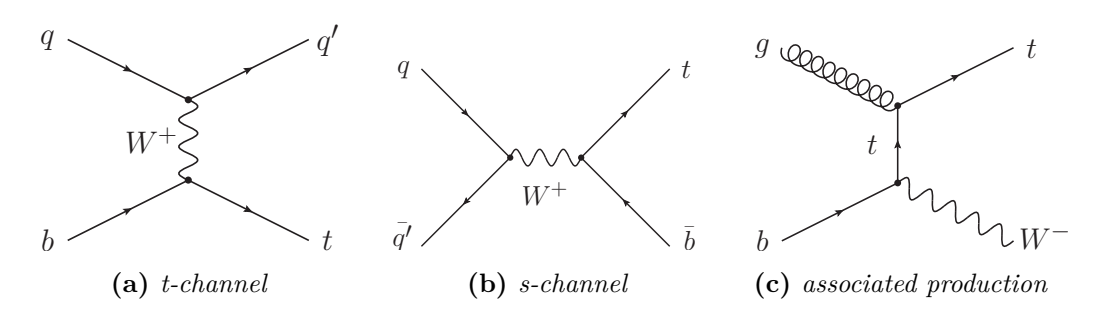


Figure 2.3: Leading-order single top-quark production modes

The calculated cross section of all three leading-order diagrams are presented in Table 2.3 [9, 10, 11]. All values have been approximated at next-to-next-to-leading-order (NNLO) precision. The high cross section of the t-channel production mode, compared to the other modes, is the reason why its investigation is the most feasible.

Even though single top-quark production via the t-channel is the most feasible to analyse, it stands against an significant amount of background processes which have identical decay signatures at a hadron collider. To improve the capability of an analysis to extract single top-quark like events, every feature of the process has to be exploited. A distinct characteristic of the t-channel process is the bottom antiquark in the final state stemming from the hard interaction. Since the top quark itself decays into a bottom quark, the other bottom antiquark is called $2^{\rm nd}$ b-quark, or spectator b.

Table 2.3: Cross sections of the three single top-quark production modes approximated at NNLO accuracy. The center-of-mass energy is $\sqrt{s} = 7$ TeVand the top-quark mass $m_t = 173$ GeV.

process	cross section [pb]
t-channel	$64.6^{+2.7}_{-2.0}$
Wt-production	15.7 ± 1.1
s-channel	4.6 ± 0.2

The calculation of the single top-quark t-channel cross section, as well as certain aspects of the process can be done in two ways. The first method is called the five-flavour-scheme, which is the $2 \to 2$ scattering process at Born level. It has two main advantages, the first is of a technical nature, since the calculation greatly simplifies. The second benefit is, that possibly large logarithms originating from the initial state gluon splitting $g \to b\bar{b}$ are consistently resummed into the b-quark parton density function.

However, the 2^{nd} b-quark enters as a radiative contribution at the next-to-leading order level, thus effectively not described at leading order. To be able to perform high-precision measurements at the LHC the description at only LO level is not satisfying.

To obtain an enhanced understanding of the $2^{\rm nd}$ *b*-quark in next-to-leading-order (NLO) precision, one must take higher-order effects into account. This approach is called four-flavour scheme. Figure 2.4 depicts three examples for these NLO corrections to the tree-level Feynman diagram. The most important correction is shown in Figure 2.4(a). This $2 \to 3$ process, at Born level, is called W-gluon fusion and is characterised by the initial-state gluon splitting into a $b\bar{b}$ pair.

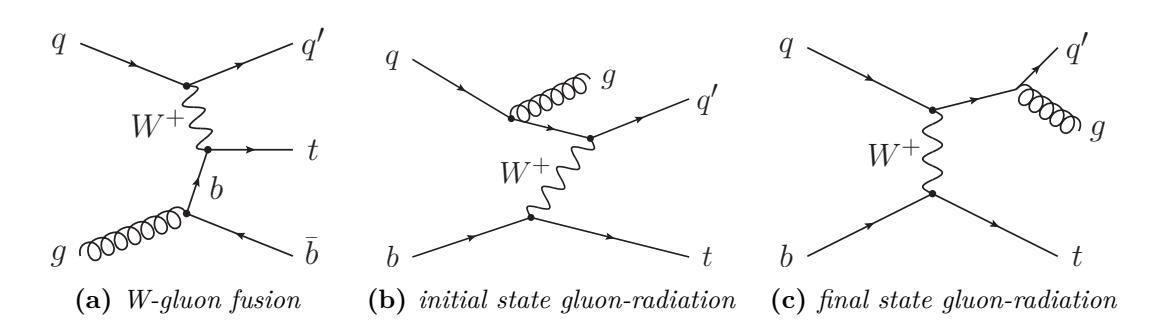


Figure 2.4: Examples for next-to-leading-order single top-quark t-channel corrections.

In the four-flavour scheme all b-quarks are considered to be massive, which entails

that the NLO-correction is much more involved due to the presence of an additional (massive) particle in the final state. However, in this scheme, the $2^{\rm nd}$ b-quark can be genuinely investigated at NLO accuracy.

Both the five- and four-flavour schemes are by definition equivalent in all orders of the pertubative expansion, yet at low order they can yield substantial different results. [12, 13]

2.4 Parton Distribution Functions

Parton is a generic name for every constituent particle of protons, neutrons and other hadrons. The constituent particles can be all six quark, plus antiquarks, as well as gluons. Gluons are binding the individual quarks together, but can produce quark-antiquark pairs, that are called sea quarks. Protons are compound objects consisting of a down-quark and two up-quarks at valence-level. When colliding protons the composition is of critical importance, since it is unknown how the momentum of the proton is distributed across all constituents. Parton distribution functions describe the momentum fraction of the individual proton constituents, as a function of the energy scale.

A description of proton-proton interactions and the correlation between the experimental cross section σ and the theoretical calculated partonic cross section $\hat{\sigma}_{a,b}$ is given by the factorisation theorem:

$$\sigma = \sum_{ab} \int dx_a dx_b f_{a/A}(x_a, Q^2) f_{b/B}(x_b, Q^2) \hat{\sigma}_{a,b} , \qquad (2.3)$$

where x_a and x_b are the fractions of momentum of the proton carried by the partons. The functions $f_{a/A}(x_a, Q^2)$ and $f_{b/B}(x_b, Q^2)$ are the Parton-Distribution-Functions that give the probability to find a parton a or b with a momentum fraction $x_{(a,b)}$ at a given momentum scale Q^2 .

Figure 2.5 illustrates the individual momentum fraction x of the constituent quarks and the gluon. The distributions are generated with the PDF set CT10 at $Q^2 = \mu^2 = 85 \text{ GeV}^2$ [14].

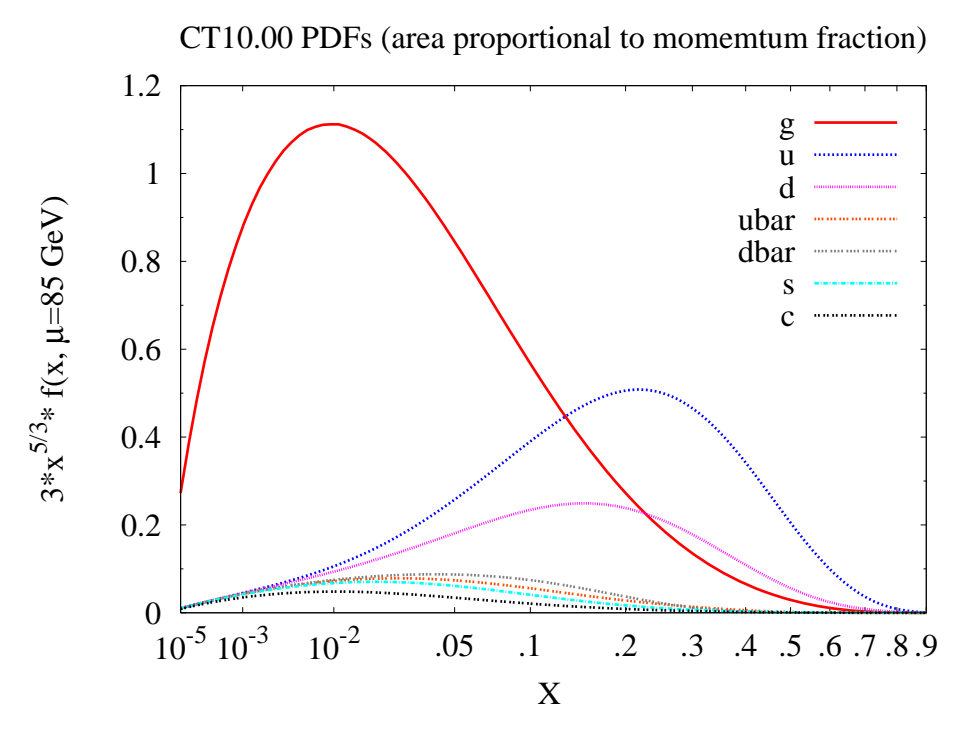


Figure 2.5: Parton distribution functions of the proton at the energy scale $Q^2 = 85 \text{ GeV}^2$. The PDF set CT10 was used to generate the distribution [14].

3 The Experimental Design

The Large Hadron Collider (LHC) is operational since 10.09.2008, when proton bunches circulated in the ring for the first time. It is located at the European Organization for Nuclear Research (CERN) near Geneva, at the border between France and Switzerland. The enormous complex is host to four major experiments, of which the A Toroidal LHC ApparatuS (ATLAS) experiment will be discussed in detail.

3.1 The Large Hadron Collider

The Large Hadron Collider is a proton-proton (pp) collider, designed to reach a maximum center-of-mass energy of $\sqrt{s}=14$ TeV, thereby exceeding every other particle accelerator so far. Besides protons, heavy-ions can be accelerated in the LHC. By design ions can reach a maximum energy-per-nucleon of 5.52 TeV. The main objective of the construction of the LHC, is to conduct searches for the Standard Model Higgs boson, to test certain Standard Model predictions at the TeVscale and to probe so far unexplored energy regimes of new physics.

The LHC has been built in the tunnel formerly occupied by the Large Electron Positron Collider (LEP). This tunnel has a circumference of about 26.7 km and several caverns for the various experiments. Figure 3.1 depicts the layout of the LHC with the major experiments ATLAS, LHC beauty (LHCb), Compact Muon Solenoid (CMS) and A Large Ion Collider Experiment (ALICE).

The instantaneous luminosity of a collider is the measure of its capability to produce physical processes. It is defined via:

$$\mathcal{L} = \frac{N_b^2 n_b f_{\text{rev}} \gamma_r}{4\pi \epsilon_n \beta^*} F \ . \tag{3.1}$$

And the integrated luminosity the therefore defined as:

$$\mathcal{L}_{int} = \int \mathcal{L} dt. \tag{3.2}$$

 N_b is the number of particles per bunch, n_b the number of bunches per beam, f_{rev} the revolution frequency, γ_r the relativistic gamma factor, ϵ_n the normalised

transverse beam emittance, b^* the beta function at the collision point, and F the geometric luminosity reduction factor due to the crossing angle at the interaction point (IP) [15]. The corresponding values taken at the end of 2011 and the nominal values of the LHC beam parameters are listed in Table 3.1 [16].

The generated number of events per time interval is given by:

$$\dot{N} = \frac{\mathrm{d}N}{\mathrm{d}t} = \mathcal{L} \cdot \sigma,\tag{3.3}$$

where σ is a specific cross section for a given process and \dot{N} is the corresponding event rate. The integrated luminosity is of key importance for the estimation of the probability that a certain process has occurred. Hence the precise knowledge of that quantity is essential. Figure 3.2 shows the evolution of the luminosity delivered by the LHC and the recorded luminosity of ATLAS in 2011.

For the experiments the delivered integrated luminosity is of utmost importance. High luminosities are needed to observe rare physics processes. The LHC is designed to generate a nominal luminosity of $\mathcal{L}=10^{34}~\mathrm{cm^{-2}~s^{-1}}$. At such high energies, electrons cannot be utilised in a synchrotron anymore. The resulting synchrotron radiation is rendering them unfeasible to accelerate at the given energies. Protons

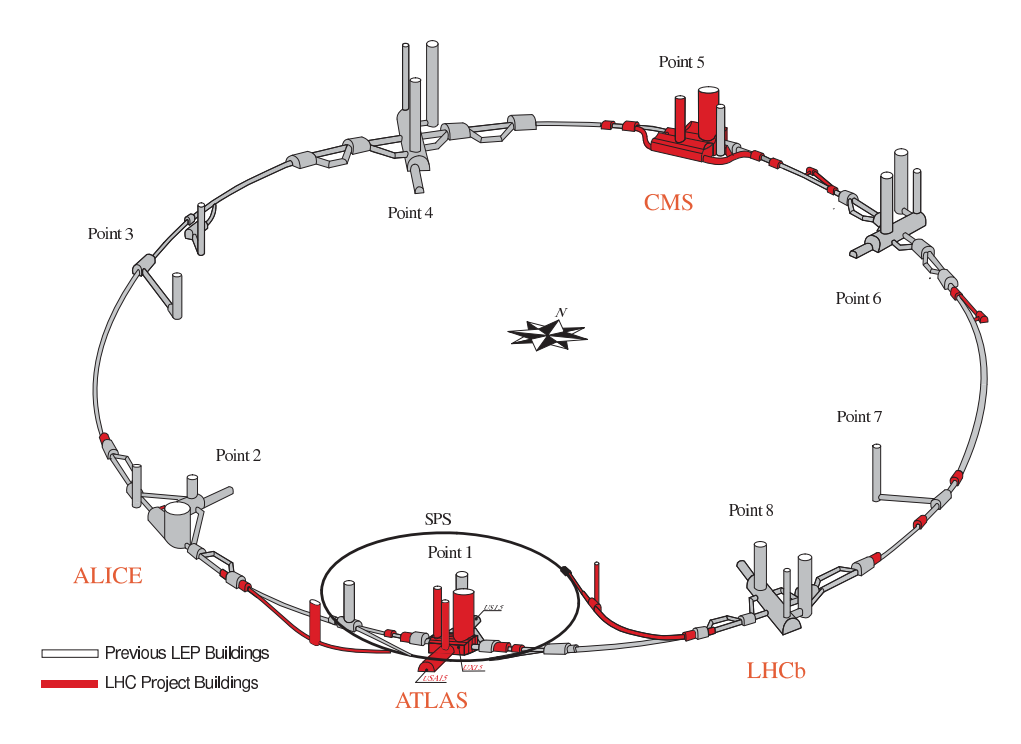


Figure 3.1: A schematic view of the LHC layout. The four main experiments are located at Point 1,2,5 and 8.

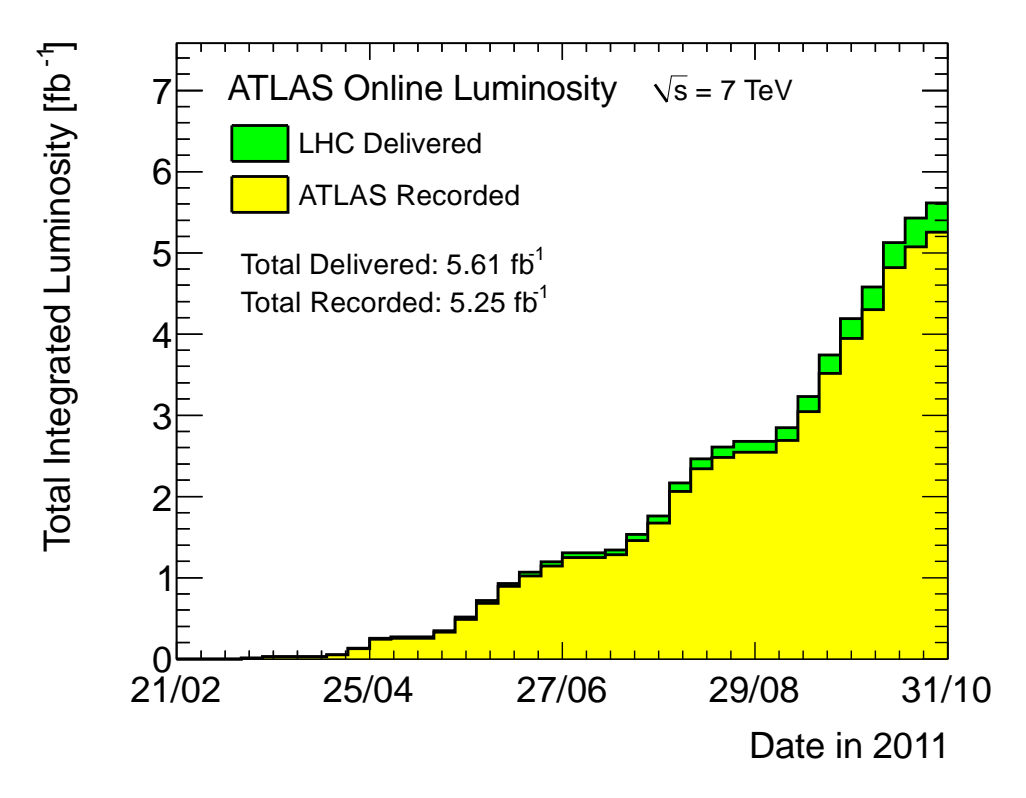


Figure 3.2: Delivered LHC luminosity and ATLAS recorded in 2011 [17].

on the other hand are much more massive than electrons and since the synchrotron radiation is proportional to $(E/m)^4$ and therefore suppressed by mass, this difficulty disappears. The protons are kept on their orbit within the vacuum-tubes, by 1232 superconducting dipole-magnets, generating magnetic field strength up to 8.33 T. All accelerated particles are grouped within bunches. 2808 of these bunches are circulating in the LHC ring, each 25 ns apart (≈ 7.5 m) by design and a 50 ns bunch spacing in 2011. The resulting design collision frequency of protons is 40 MHz whereas in 2011 20 MHz are used. Each bunch contains on average $N_b = 1.15 \cdot 10^{11}$ protons nominal and $N_b = 1.5 \cdot 10^{11}$ in 2011.

In a single collision 30 inelastic interactions take place on average, and about 1000 new particles are created. The detection and observation of the created particles and their decay, is the task of the four particle detectors: ATLAS, LHCb, CMS and ALICE.

A series of pre-accelerators increase the energy of either protons or heavy-ions step-by-step. In the proton case a linear accelerator and a booster are initially providing the collision objects, whereas the low energy ion ring (LEIR) accelerator is delivering heavy-ions. The next step for protons, is the Proton Synchrotron (PS), which increases their energy from 1.4 to 25 GeV. Afterwards, injected into the Super

Parameter	2011	Nominal
$N (10^{11} \text{ p/b})$	1.5	1.15
$k (n_{bunches})$	1380	2808
Bunch spacing (ns)	50	25
$\epsilon \; (\mu \mathrm{m} \; \mathrm{rad})$	1.9-2.3	3.75
β^* (m)	1	0.55
$L (cm^{-2} s^{-1})$	$3.6 \ 10^{33}$	10^{34}
Energy (MJ) stored	110	360

Table 3.1: Parameters of LHC exploitation, at the end of 2011, and design parameters at 14 TeV in the centre of mass [16].

Proton Synchrotron (SPS), the energy reaches 450 GeV, when entering the LHC ring. Two different transfer lines from the SPS are used to supply the protons for both beam directions in the LHC.

In 2012, the center-of-mass energy has been raised from 7 TeV in 2011 to 8.0 TeV. The maximum design beam-energy is 7 TeV, which will be reached in a few years.

3.2 The ATLAS Detector

In this section the ATLAS detector will be discussed in detail. The purpose of this detector is to be able to encompass a wide range of physical processes. As already mentioned, the search for the Higgs boson is of top priority, but other tests of Standard Model predictions and various searches of new physics are performed at the ATLAS experiment as well.

The detector is located within a cavern at the LHC ring (cf. Figure 3.1). It is the biggest of the four main experiments with a length of 44 m, a diameter of 25 m and a weight of about 7000 t. Figure 3.3 shows a graphical representation of the detector.

As the whole spectrum of particles needs to be measured, one must take different types of interactions into account. In order to measure different quantities of particles multiple detectors are necessary. To incorporate a variety of measurement equipment, the ATLAS detector is constructed in a layered fashion. Each layer is capable of measuring distinct quantities of the produced particles. The hierarchy is determined by the range of each particle type and thus the interaction.

The ATLAS coordinate system is right-handed and has its origin at the designed interaction point. The x-axis is pointing towards the center of the LHC, the z-axis is the tangent of the beampipe at the interaction point. The azimuthal angle ϕ is measured from the x-axis in the x-y plane. The polar angle θ is measured

from the z-axis. The rapidity is used instead of the polar angle, and is defined as:

$$y \equiv \frac{1}{2} \ln \left(\frac{E + p_z}{E - p_z} \right) \tag{3.4}$$

or the pseudorapidity is used:

$$\eta \equiv -\ln\left(\tan\left[\frac{\theta}{2}\right]\right) \tag{3.5}$$

The angular distance is defined as:

$$\Delta R \equiv \sqrt{(\Delta \eta)^2 + (\Delta \phi)^2} \tag{3.6}$$

For objects that are measured in the calorimeter, like hadronic jets, the transverse energy is defined as:

$$p_{\rm T} \equiv \sqrt{p_x^2 + p_y^2}, \qquad E_{\rm T} \equiv E \cdot \sin(\theta)$$
 (3.7)

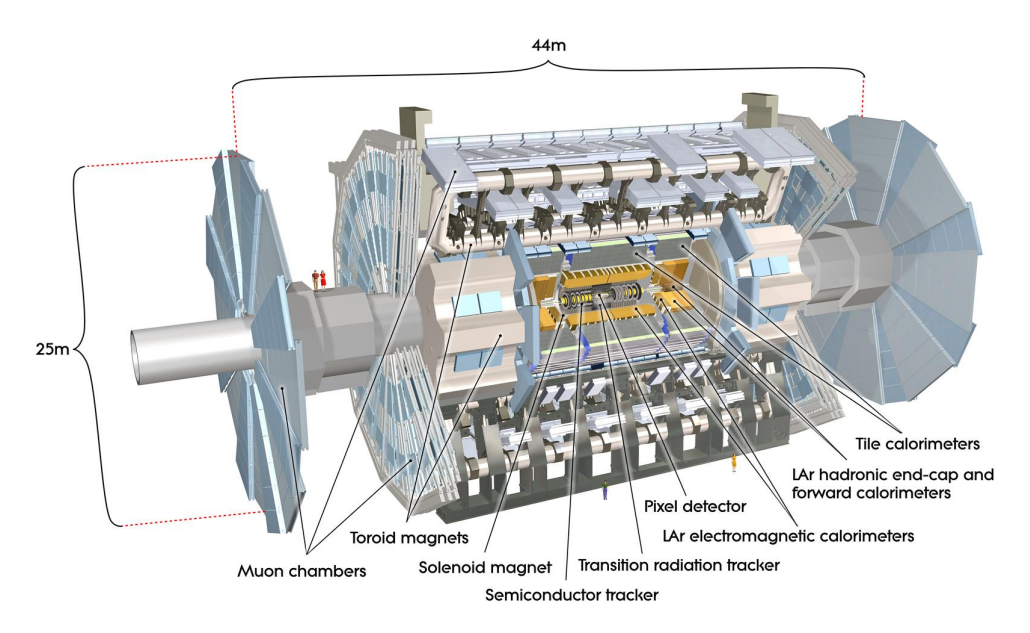


Figure 3.3: Cut-away view of the ATLAS detector. The dimensions of the detector are 25 m in height and 44 m in length [17].

3.2.1 Luminosity Detectors

Within the ATLAS Detector, different sensors are used to determine the bunch-by-bunch luminosity. The first is LUCID, it is a Cerenkov detector specifically designed for the ATLAS luminosity measurement. There are 16 polished aluminum tubes, containing C_4F_{10} gas enveloping the beampipe on both sides of the interaction point with a distance of 17 m. A pseudorapidity region $5.6 < |\eta| < 6.0$ is covered. Photomultipliers at the end of each tube detect cerenkov photons, which are created by charged particles in the gas, transversing faster than the speed of light in the respective gas. LUCID provides a signal, if a detected photon passes a certain threshold and it is than aligned with the LHC clock to coincide with a given bunch crossing ID (BCID).

The Beam Conditions Monitor (BCM) is the second detector measuring the bunch-by-bunch luminosity at ATLAS. The BCM has four diamond sensors attached to the beamline in a cross pattern. The primary function of the BCM is to monitor background and initiate a beam-abort in case beam-losses threaten to damage the ATLAS detectors. More information on the luminosity measurement can be obtained from [18].

3.2.2 The Inner Detector

The innermost detector of ATLAS is the Inner Detector (ID), depicted in Figure 3.4. The ID provides charged particle tracking over a pseudorapidity range $|\eta| < 2.0$ and a wide sector of energies between 0.5 GeV and 150 GeV. The ID is pervaded by a 2 T solenoidal magnetic field. The magnetic field is essential for the momentum measurement which depends on the curvature of the tracks.

The Pixel Detector is a part of the ID located at 50.5 to 122.5 mm from the beam axis, shown in Figure 3.4. The purpose of the Pixel Detector, is to measure tracks of charged particle produced in the hard proton collision or decay products of primary particles. The Pixel Detector is made up of 1744 modules and consists of 80 million pixels in total. It is divided into three sections, the barrel and the end-cap sections, each consisting of three layers. By design, it supplies three spacepoints for each charged track within a pseudorapidity region $|\eta| < 2.5$. The spacial resolution of the Pixel Detector is $10 \times 115~\mu m$ in $R \cdot \varphi$ and z. The vertex resolution is with 12 μm in x,y suited for high precision separation of multiple primary vertices. A vital task for the Pixel Detector is to enable the identification of b-quark jets, which will be discussed later.

The second layer of the Inner Detector is the SemiConductor Tracker (SCT), 299-554 mm from the beam axis. It is designed to measure eight spacepoints per track, which are used to determine the momenta, impact parameters of tracks as

well as vertex positions. In the barrel region the SCT has eight layers of silicon microstrip detectors. In Figure 3.5 a 10 GeV track which traverses the sensors and structures of the SCT and the other Inner Detector modules is depicted. Due to the lower granularity of the SCT, the final precision of the track measurement is reached, when combined with tracks from the pixel volume. The intrinsic accuracies per module in the barrel are 17 μ m ($R \cdot \varphi$) and 580 μ m in z.

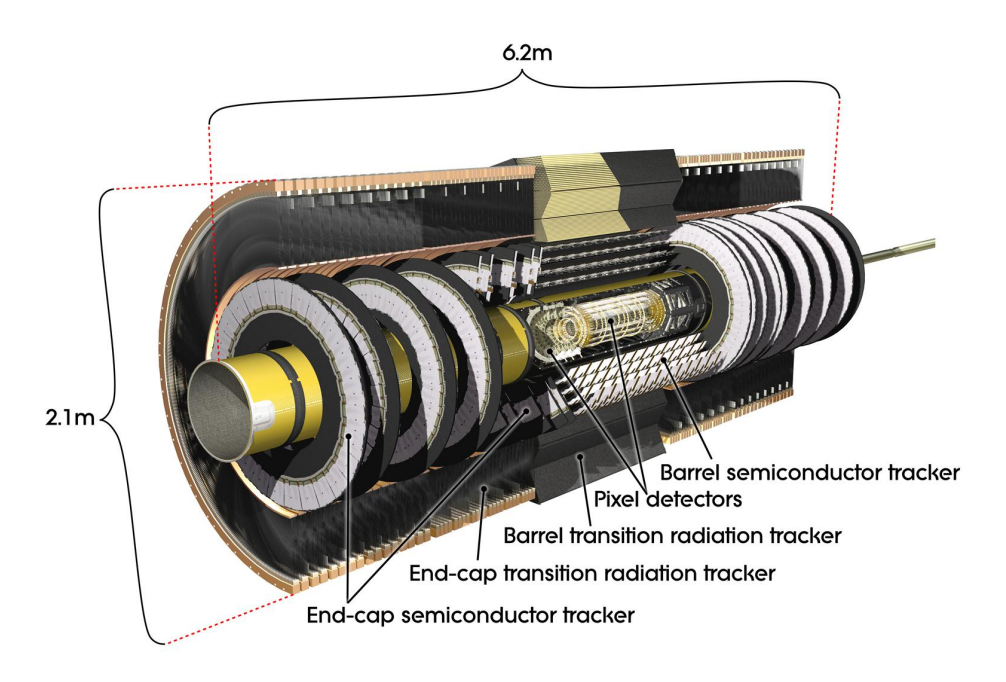


Figure 3.4: The ATLAS Inner Detector layout. Parts of TRT and SCT has been removed to show inside objects [17].

The third and last layer is the Transition radiaton Tracker (TRT), which completes the Inner Detector located at 554-1082 mm from the beam axis. Essentially, it is made of small diameter straw detectors, each containing an individual gas volume and a sense wire. Each straw is 2 mm in radius and contains a 30 μ m diameter gold-plated W-Re wire. The enclosed gas is composed of 70% Xenon, 27% CO₂ and 3% O₂, and is used to detect transition radiation photons. The photons are created in a radiator between two straws [19].

Table 3.2 contains the measured momentum corrections between the Monte Carlo modelling and data of the Inner Detector, for different p_T and η regimes [20]. For a pseudorapidity region from $-1.2 < \eta < 1.2$ for high p_T tracks, the accuracy is high, but even in high η regimes for low p_T tracks agreement between the model and data is good.

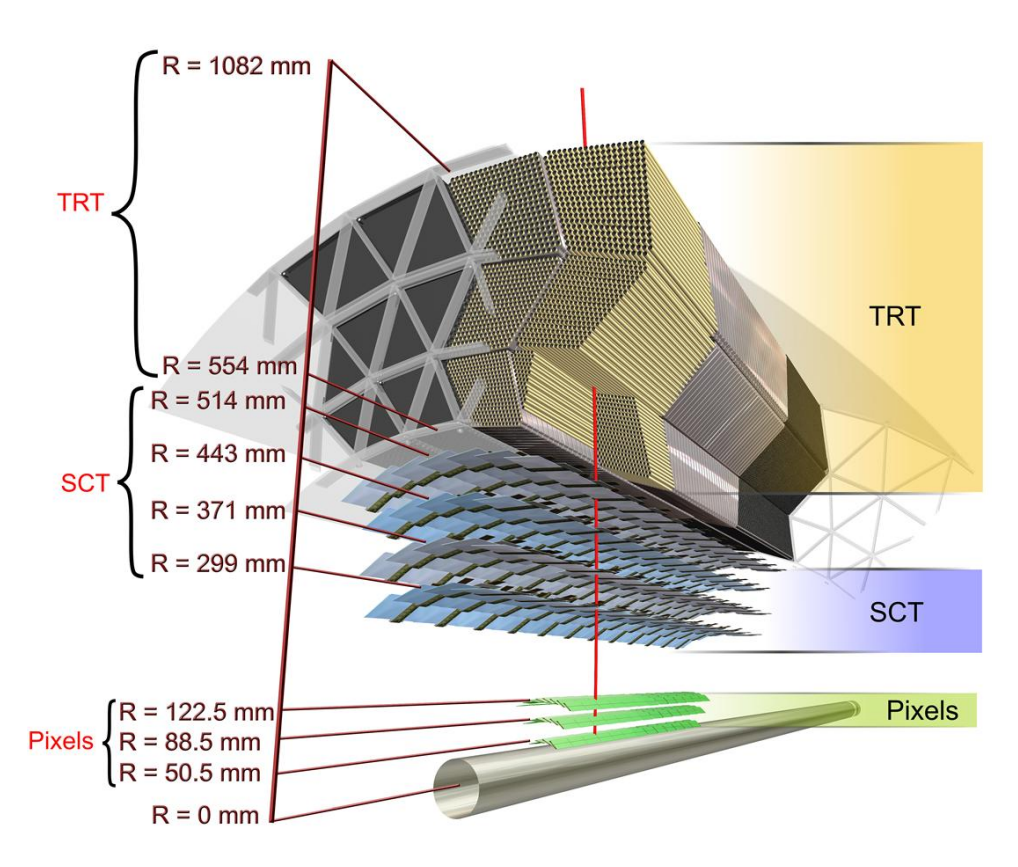


Figure 3.5: The picture is showing the sensors and structural elements traversed by a charged track of 10 GeV p_T in the barrel Inner Detector ($\eta = 0.3$) [17, 19].

Table 3.2: Momentum scale (top) and additional resolution σ (bottom) parameters for the different p_T and η regimes. The uncertainties are statistical only [20].

$Scale(\mu)$	$\eta < -1.2$	$-1.2 < \eta < 1.2$	$\eta > 1.2$
$p_T < 500 \text{ MeV}$ $p_T > 500 \text{ MeV}$	0.998 ± 0.001 0.999 ± 0.001		$1.001 \pm 0.002 \\ 1.000 \pm 0.002$
Add. resolution (σ)	$\eta < -1.2$	$-1.2 < \eta < 1.2$	$\eta > 1.2$
$p_T < 500 \text{ MeV}$ $p_T > 500 \text{ MeV}$	0.024 ± 0.004 0.00 ± 0.01	0.001 ± 0.008 0.004 ± 0.002	0.022 ± 0.004 0.015 ± 0.008

3.2.3 Calorimeter

A calorimeter system is a device which measures the energy of a given particle. In general only neutrinos and muons are capable of passing through the calorimeter system, due to their physical properties. Figure 3.6 depicts the calorimeter system of the ATLAS detector. In case of the ATLAS detector the calorimeter system consists of two distinct sampling calorimeters, with full ϕ -symmetry. Sampling calorimeters consist of two alternating materials, the first is the stopping material, preferably with a high charge number for the hadronic calorimeter, in which penetrating particles quickly loose their energy. When a particle is stopped in the first layer, secondary particles are produced which lead to charge imbalances in the second layer, which can be detected. The resulting electronic pulse measured in the detecting layer is proportional to the energy of the initial particle.

The first part of the calorimeter is the electromagnetic calorimeter, designed to measure the energy of electrons and photons in the pseudorapidity region of $|\eta| < 2.5$ with high precision and $2.5 < |\eta| < 3.2$. Additionally the forward calorimeter (FCal) provides electromagnetic coverage from $3.1 < |\eta| < 4.9$. Studies of the electron energy measurement yield an relative accuracy of $3 \cdot 10^{-4}$ within the range 10 < E < 180 GeV [21].

The electromagnetic calorimeter is the innermost part of the calorimeter system. The stopping material in this case is lead, due to its high charge number. Liquid argon is used as the active detector medium in the barrel region.

The hadronic calorimeter has the purpose to measure the energy of mesons and baryons formed from quarks which have been produced in the hard collision, as well as secondary decay products. It is subdivided into three sub-detectors covering different pseudorapitity regions. The sub-detector, which covers the barrel-region and extended barrel-region, is the tile calorimeter (0 < $|\eta|$ < 1.7). For greater pseudorapidities the hadronic calorimeter is extended by the hadronic end-cap calorimeter (HEC).

The stopping material of the hadronic calorimeter is made of steel in the barrel region, and copper as well as tungsten in the end-cap region. The barrel and extended barrel calorimeters use iron plates as absorber and scintillating tiles as active material. The front-end electronics also provide analogue sums of subsets of the channels, forming trigger towers, for the Level 1 trigger, which is discussed later.

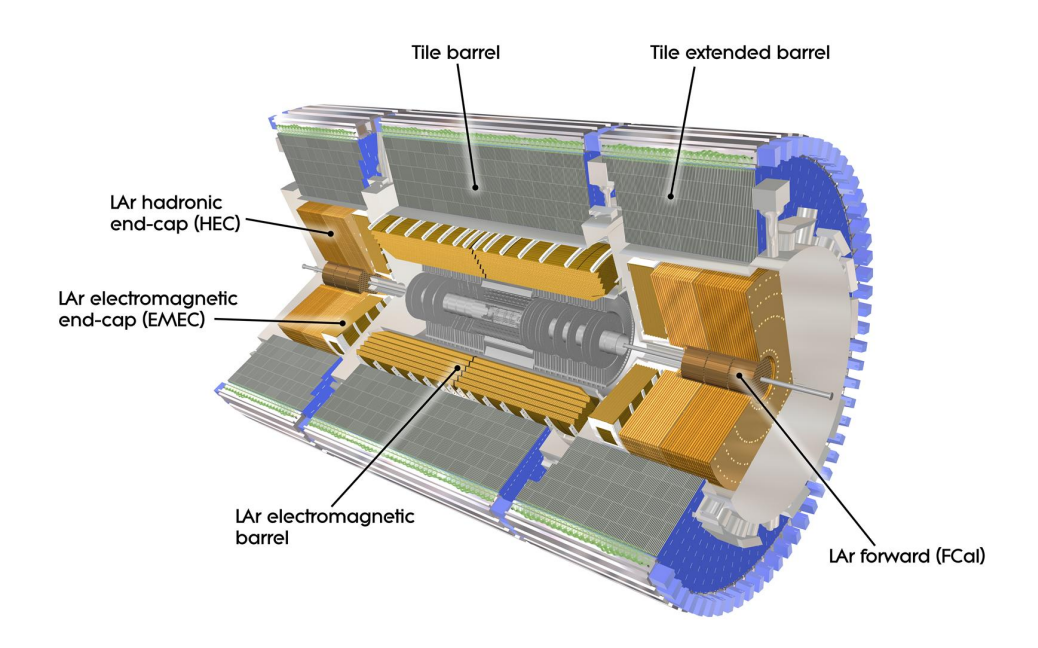


Figure 3.6: The ATLAS calorimeter system. Removed parts allow to see the inner electromagnetic subsystem and the forward calorimeter [17].

3.2.4 Muon Spectrometer

The muon spectrometer forms the outermost part of ATLAS. It is designed to identify muons and determine their charge, as well as their momentum in a pseudorapidity region of $|\eta| < 2.7$. The muon system is also capable to trigger on muons within a pseudorapidity region of $|\eta| < 2.4$. One performance goal of the muon system, is to achieve a transverse momentum resolution of a 1 TeV muon track to be 10%.

Figure 3.7 shows a cut-view of the muon system. The charge measurement as well as the momentum measurement, is accomplished by using a toroid magnetic field, with a strength reaching from 0.5 to 2.0 T. This field is generated by eight superconducting toroidal magnets in the barrel region and two end-cap toroid magnets, in the forward region.

Four different detector types are used in the muon spectrometer:

- Monitored Drift Tubes (MDT): Perform precision momentum measurements, with a resolution of 35 μm .
- Resistive Plate Chambers (RPC): Fast tracking chambers with coarse-grained resolution. They provide φ -information for the MDTs and provide trigger information. The resolution is 10 mm in z and 10 mm in φ .
- Thin Gap Chambers (TGC): Replace the functionality of the MDTs in the endcap region and are also used for trigger-purposes. The resolution is 2-6 mm in R and 3-7 mm in ϕ .
- Cathode Strip Chambers (CSC): Replace the function of the TGS in the forward muon chambers, but are not part of the trigger system. The resolution is 40 μ m in R and 5 mm in ϕ .

The ATLAS muon system has been subject to performance and efficiency measurements, yielding a muon reconstruction efficiency of > 96%, as well as an agreement with the Monte Carlo prediction below 1% [22].

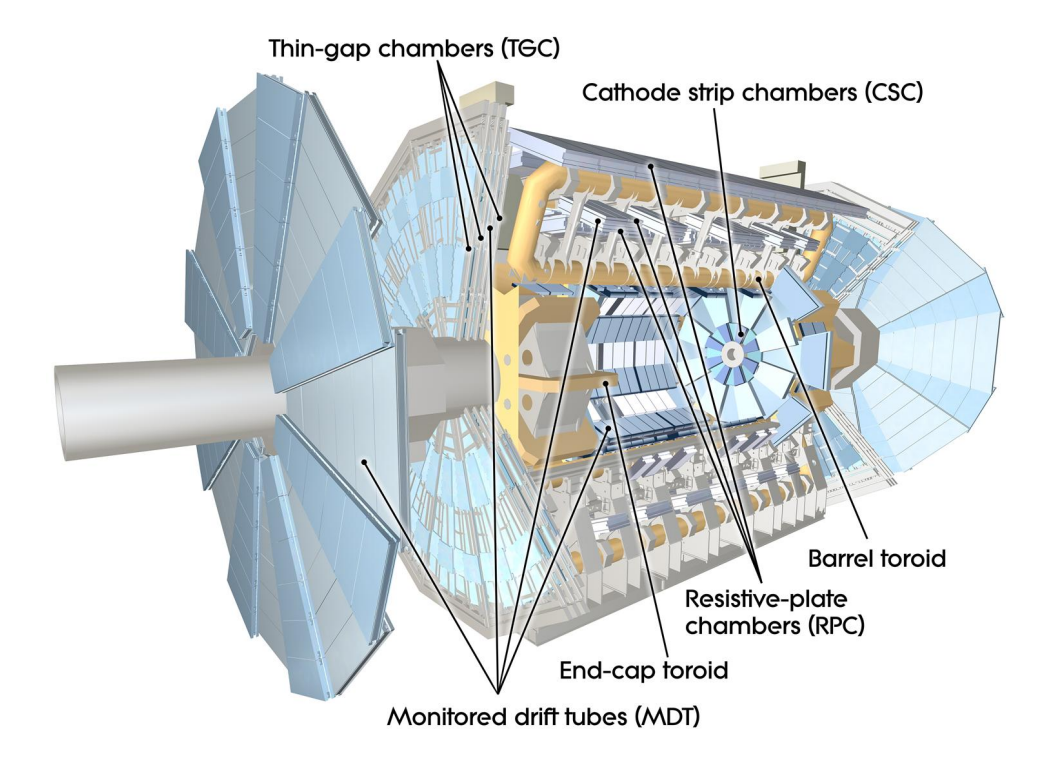


Figure 3.7: A cut-view of the Muon System [17].

3.2.5 Trigger System

The ATLAS Trigger System has the purpose of pre-filtering events, to reduce the amount of raw data to an event rate that can be handled by the data processing hardware. Figure 3.8 shows a schematic overview of the trigger system. As discussed in section 3.1, the bunch-crossing rate and therefore the interaction-rate is 40 MHz. With state-of-the art technology event-rates of 600 Hz can be saved and analysed in detail [23]. The difficulty arises from preserving the relevant physics processes, while discarding only background.

The ATLAS Trigger System consists of three sequential trigger stages. The first is the Level-1 trigger (L1), then the Level-2 trigger (L2) and the Event Filter. The hardware of the L1 trigger is custom made, while the L2 trigger and the Event Filter are software based and run on computer farms.

The L1 trigger is evaluating signatures from high- p_T muons, jets, electrons/photons and τ -leptons decaying into hadrons. The L1 trigger selects events with large total transverse energy and considerable missing transverse momentum (\rlap/E_T).

The L2 trigger is seeded by Regions of Interest (ROI). ROIs are derived from the information provided by the L1 trigger. The L2 trigger is utilising energy, coordinates and other information obtained by the L1 trigger to pre-select data needed to be transferred from the detector readout. The L2 trigger is capable to decrease the event rate from 75 kHz to about 3.0 kHz.

If an event passes the L2 trigger stage, it is fully reconstructed and transferred to the Event Filter. Algorithms are in place, which are seeded by the L2 trigger results, and after an event has been positively evaluated, it is send to mass-storage. The final event rate can be reduced, by all three trigger stages, to about 600 Hz and over six orders of magnitude [24].

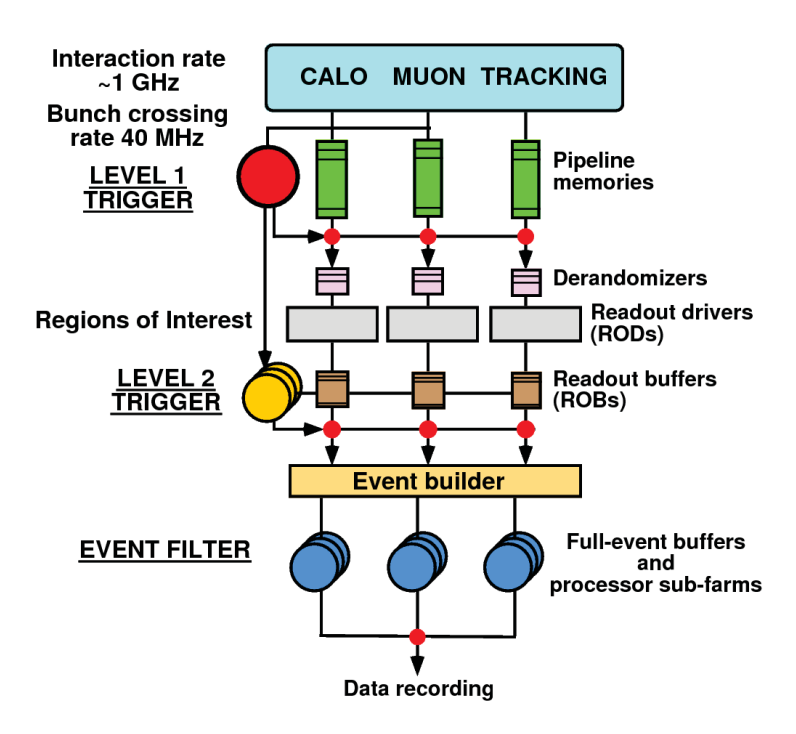


Figure 3.8: Schematic overview of the ATLAS trigger system. It consists of three trigger stages, L1,L2 and the Event Filter.

4 Monte Carlo Methods

A particle physics analysis is set up on a convoluted groundwork. In this chapter the concepts and analytical tools are introduced. In particle physics a precise theoretical model is required to match the measured data. The complexity of the phenomena, that are desired to investigate by the LHC, is exceeding the capabilities of a quantum mechanical description. Fortunately the computing power has increased to a point, where numerical approximations are feasible for many applications.

4.1 Monte Carlo Simulation

Monte Carlo (MC) Simulation has become the standard technique in particle physics, to evaluate complex mathematical problems. To mimic all aspects of the signal-and background-process behaviour, Monte Carlo methods are used. MC models are fundamentally dependent on the precise knowledge of the physics of the process in question.

The cross section of a given process is calculated via:

$$\sigma = \sum_{ab} \int dx_a dx_b f_{a/A}(x_a, Q^2) f_{b/B}(x_b, Q^2) \hat{\sigma}_{a,b} , \qquad (4.1)$$

where $x_{a(b)}$ is the momentum fraction of the respective parton and $f_{a/A}(x_a, Q^2)$ is the parton distribution function for parton a and b. The calculated cross section is introduced by $\hat{\sigma}$. In order to solve these types of equations, numerical methods are needed, since the integrals are high-dimensional and no analytical solution can be obtained.

Basically all MC simulations are designed to solve integrals in the form of

$$I = \int_{x_1}^{x_2} f(x)dx = (x_2 - x_1)\langle f(x)\rangle$$
 (4.2)

To obtain the average value of the function f(x) one can use the definition for the arithmetic mean:

$$I \approx I_N \equiv (x_2 - x_1) \frac{1}{N} \sum_{i=1}^{N} f(x_i)$$
 (4.3)

This numerical approximation of the mean value of the function f(x) can now be easily calculated, by drawing a large number of random values for i. Furthermore one can use the Central Limit Theorem to obtain an error on that approximation:

$$I \approx I_N \pm \sqrt{V_N/N} \tag{4.4}$$

where
$$V = (x_2 - x_1) \int_{x_1}^{x_2} [f(x)]^2 dx - \left[\int_{x_1}^{x_2} f(x) dx \right]^2$$
 (4.5)

This error approximation is only valid for MC integrals governed by the Central Limit Theorem.

4.1.1 Branches of Monte Carlo Event Generators

The production of a viable model of the physics processes at the LHC, is subdivided into different parts of simulation. Figure 4.1 depicts the different steps in which MC Simulation is partitioned. Besides predicting the characteristics of all objects emerging from the hard interaction, a MC generator must provide the quantities that can be measured by the detector. The evolution of an unstable particle from its production to its hadronisation and decay is simulated in steps.

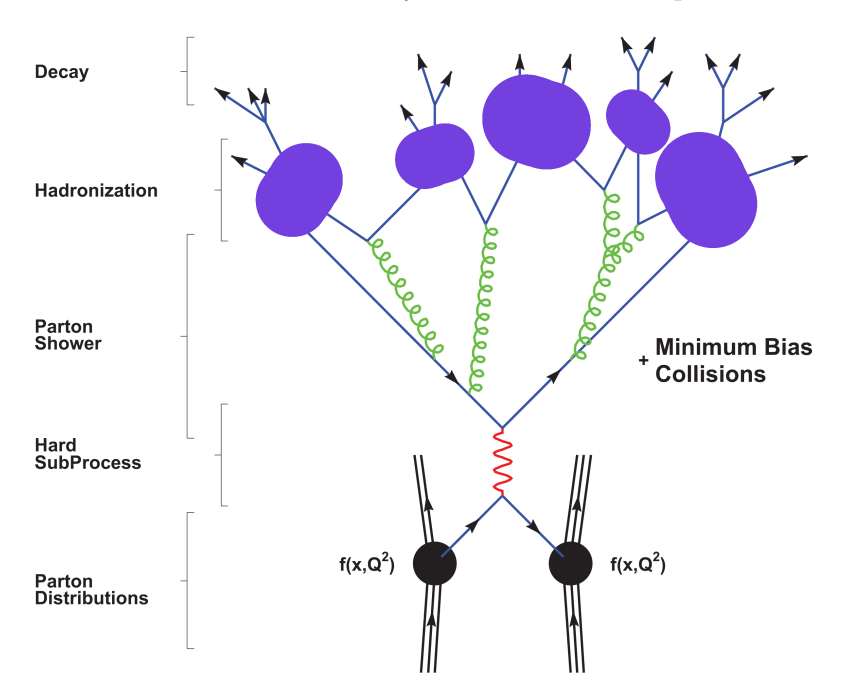


Figure 4.1: The basic structure of a showering and hadronisation generator event is shown schematically [25].

Parton Distribution

At the time of the collision of two hadrons, the momentum distribution amongst its constituents is described by the parton density function, as mentioned in section 2.4. The momentum fraction x and thus the energy that is available for the physical process is the determined by this part of the simulation.

Hard Process

The hard process is the main interaction between the partons of each hadron. It is described by Feynman graphs and calculated applying the Feynman rules to all diagrams of the process in question, yielding the Feynman amplitude \mathcal{M} . The differential cross section $d\sigma/d\Omega$ is proportional to the squared magnitude of the matrix element $|\mathcal{M}|^2$. Monte Carlo methods are used to perform the neccesary integration, by sampling the high-dimensional phase space with random numbers.

Parton Shower

The hard process involves high momentum transfers, which in case of coloured objects result in QCD radiation. The parton shower includes gluon radiation in the initial- and final state to the simulation, as well as other higher order corrections. It is however not feasible to calculate the exact corrections, instead approximation schemes are used. The dominating corrections are associated with collinear parton splitting or soft gluon emission. The branching of partons is described by the PDF, as described in Section 2.4.

Hadronisation

The coupling constant α_s of the strong force is a scale dependant quantity, which increases with low values of the shower evolution scale. At a certain point of the evolution perturbation theory will be rendered invalid. Event generators therefore have to rely on models based on general features of QCD. In the hadronisation step, the quarks which are present after the showering step are grouped in colour neutral objects. Two models exist for the hadronisation process, the cluster model for one, selects the colour neutral groups by proximity and the string model which is emulating the quark confinement.

Hadron Decays

The final stage of the event generator is the decay of unstable hadrons, which have been bound in the hadronisation step.

Underlying Event and Pile-up

Since hadrons are compound objects, the hard interaction leaves out constituents which themselves can engage in interactions with partons from the second hadron. These events, which arise from collisions of the remaining partons not participating in the hard process, are called underlying event.

Due to the number of protons in a bunch, the probability of multiple protons engage in interaction is not negligible. Pile-up events are those events which arise from collisions of protons not affiliated with the hard process.

4.1.2 Monte Carlo Generators

In this section are the used Monte Carlo generators briefly introduced. Several different MC event generators are available.

MC@NLO

The MC@NLO generator has the following features: fully exclusive events are generated, with hadronisation according to the MC model; total exclusive rates are accurate to NLO; NLO results for distributions are recovered upon expansion in α_s ; hard emissions are treated as in NLO computations while soft/collinear emissions are handled by the MC simulation, with the same logarithmic accuracy as the MC; and matching between the hard- and soft/collinear-emission regions is smooth. [26]

Herwig

HERWIG is a general-purpose Monte Carlo event generator, which includes the simulation of hard lepton-lepton, lepton-hadron and hadron-hadron scattering and soft hadron-hadron collisions in one package. It uses the cluster parton-shower approach for initial- and final-state QCD radiation, including colour coherence effects and azimuthal correlations both within and between jets. [27]

Pythia

The PYTHIA program is a standard tool for the generation of high-energy collisions, comprising a coherent set of physics models for the evolution from a few-body hard process to a complex multi-hadronic final state. It contains a library of hard processes and models for initial- and final-state parton showers, multiple parton-parton interactions, beam remnants, string fragmentation and particle decays. [28] The Lund model is implemented for hadronization [29].

AcerMC

The AcerMC Monte Carlo generator provides a library of the massive matrix elements and native phase space modules for generation of a set of selected processes. The hard process event can be completed by the initial and final state radiation, hadronisation and decays through the existing interface with either Pythia or Herwig. [30]

POWHEG BOX

The Powheg Box is a general computer framework for implementing NLO calculations in shower Monte Carlo programs according to the POWHEG method which entails the generation of the hardest gluon emission first and then subsequently adding a 'truncated' shower before the emission. [31]

Alpgen

ALPGEN is a event generator dedicated to the study of multi-parton hard processes in hadronic collisions. The code performs, at the leading order in QCD and electroweak interactions, the calculation of the exact matrix elements for a large set of parton-level processes of interest in the study of the Tevatron and LHC data. [32]

4.1.3 Used MC samples

In this Thesis a set of MC samples are used. In Table 4.1 the dijet PYTHIA samples are listed. The samples are subdivided according to the jet multiplicity of the generated event. Since events containing four jets are far less likely as a single jet event and in order to ensure sufficient event statistics it is necessary to generate each jet multiplicity seperately. The samples with dataset numbers xx80xxx are produced like the samples with dataset number xx50xxx, but involve an event filter which significantly increases the b-flavour event fraction.

Table 4.2 and 4.3 contains used MC samples for single top-quark analyses, subdivided in top-quark processes and other Background processes. The cross section is given as well as the k-factor which is a correction for LO to NLO calculations. The generator as well as the respective shower models are listed and the total number of events in each MC sample.

 ${\sf Table~4.1:~Pythia~} \textit{dijet~MC~} sample, \textit{subdivided~} \textit{by jet~} \textit{multiplicities}.$

Jet slice	Dataset Number	σ [pb]	Total Events
1jet	108067	$8.0699 \cdot 10^5$	1784489
2jet	108068	$4.8028 \cdot 10^4$	1402939
3jet	108069	$2.5360 \cdot 10^3$	950772
4jet	108070	$9.9614 \cdot 10^{1}$	965709
1jet	105010	$8.0726 \cdot 10^5$	1385247
2jet	105011	$4.8048 \cdot 10^4$	1387264
3jet	105012	$2.5369 \cdot 10^3$	1397955
4jet	105013	$9.9608 \cdot 10^{1}$	1397398

Table 4.2: Top quark MC samples, for single top quark production and $t\bar{t}$.

	σ [pb]	k-factor	Generator	Total Events
W + t-channel all decays	15.74	1.0	AcerMC+Pythia	300,000
t-channel $(e+jets)$	6.94	1.0	ACERMC+PYTHIA	200,000
t-channel $(\mu+jets)$	6.83	1.0	ACERMC+PYTHIA	200,000
t -channel $(\tau + \text{jets})$	7.26	1.0	ACERMC+PYTHIA	200,000
s-channel (e +jets)	0.498	1.0	ACERMC+PYTHIA	200,000
s-channel $(\mu+jets)$	0.489	1.0	ACERMC+PYTHIA	200,000
s-channel $(\tau+jets)$	0.521	1.0	ACERMC+PYTHIA	200,000
$t\bar{t}$ no fully hadronic	79.01	1.146	MC@NLO+HERWIG	15,000,000

Table 4.3: Background MC samples for single top-quark analyses.

	σ [pb]	k-factor	Generator	Total Events
$Z \to \ell\ell + 0 \text{ parton}$	668	1.25	Alpgen+Herwig	6,620,000
$Z \to \ell\ell + 1$ parton	134	1.25	ALPGEN+HERWIG	1,335,000
$Z \to \ell\ell + 2$ partons	41	1.25	Alpgen+Herwig	405,000
$Z \to \ell\ell + 3$ partons	11	1.25	Alpgen+Herwig	110,000
$Z \to \ell\ell + 4$ partons	2.9	1.25	Alpgen+Herwig	30,000
$Z \to \ell\ell + 5 \text{ partons}$	0.8	1.25	ALPGEN+HERWIG	10,000
$W \to \ell\nu + 0 \text{ parton}$	6,920	1.2	Alpgen+Herwig	3,460,000
$W \to \ell \nu + 1$ parton	1,303	1.2	Alpgen+Herwig	642,000
$W \to \ell \nu + 2 \text{ partons}$	380	1.2	Alpgen+Herwig	3,770,000
$W \to \ell \nu + 3 \text{ partons}$	100	1.2	Alpgen+Herwig	1,010,000
$W \to \ell \nu + 4 \text{ partons}$	26	1.2	Alpgen+Herwig	250,000
$W \to \ell\nu + 5 \text{ partons}$	7	1.2	ALPGEN+HERWIG	70,000
$W \to \ell \nu + b\bar{b} + 0$ parton	47	1.2	ALPGEN+HERWIG	475,000
$W \to \ell \nu + b\bar{b} + 1$ parton	36	1.2	Alpgen+Herwig	360,000
$W \to \ell\nu + b\bar{b} + 2$ partons	17	1.2	Alpgen+Herwig	175,000
$W \to \ell \nu + b\bar{b} + 3 \text{ partons}$	7	1.2	ALPGEN+HERWIG	70,000
$W \to \ell \nu + c\bar{c} + 0$ parton	128	1.2	Alpgen+Herwig	1, 275, 000
$W \to \ell \nu + c\bar{c} + 1$ parton	105	1.2	Alpgen+Herwig	1,050,000
$W \to \ell\nu + c\bar{c} + 2$ partons	52	1.2	Alpgen+Herwig	525,000
$W \to \ell\nu + c\bar{c} + 3$ partons	17	1.2	ALPGEN+HERWIG	170,000
$W \to c + 0$ parton	644	1.52	Alpgen+Herwig	6,500,000
$W \to c + 1$ parton	205	1.52	Alpgen+Herwig	2,070,000
$W \to c + 2$ partons	51	1.52	ALPGEN+HERWIG	520,900
$W \to c + 3$ partons	11	1.52	ALPGEN+HERWIG	115,000
$W \to c + 4$ partons	3	1.52	ALPGEN+HERWIG	30,000
\overline{WW}	11.5	1.48	HERWIG	250,000
WZ	3.46	1.6	HERWIG	250,000
ZZ	0.97	1.3	HERWIG	250,000

4.2 Detector Simulation

After a MC event generator has calculated the final state objects which can be measured in the detector, the precise detector response needs to be evaluated. The interaction between the particles and the sensors as well as the passive material has to be incorporated into a model of the detector. Figure 4.2 illustrates the stages of the detector simulation. The left path illustrates the actual measured data, while the right path illustrates the simulation output. The event reconstruction does not distinguish between either path, the detector simulation must therefore provide a compatible output to the detector output. The detector simulation at ATLAS is performed by the GEANT4 package [33].

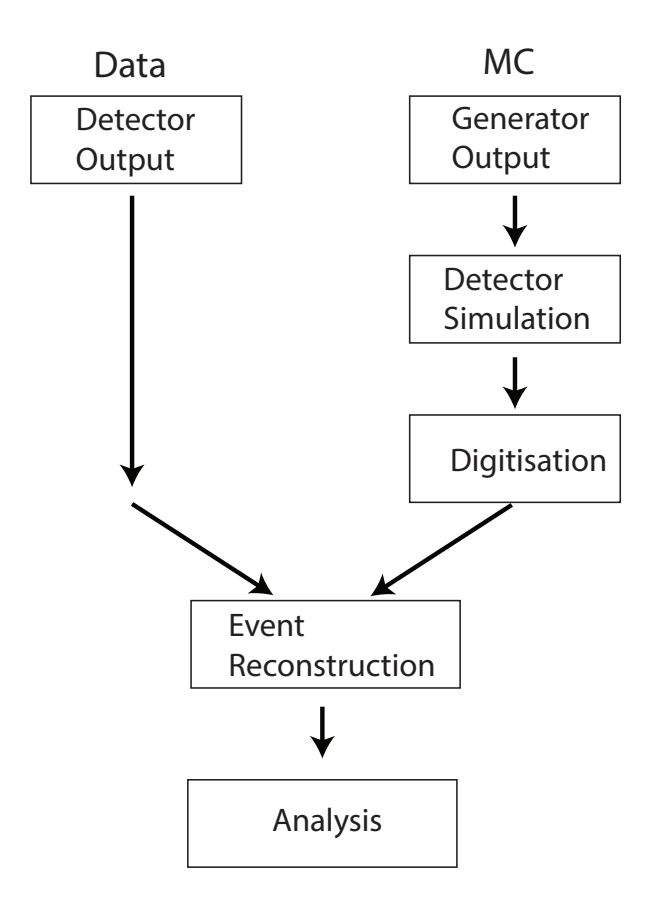


Figure 4.2: Stages of the combination of simulated data and real data. Subdivided in the measured data path and the simulated MC path to be joined in the event reconstruction.

5 Kinematic Studies

In this Chapter studies on theoretical predictions at the parton level of the single top-quark t-channel are conducted. Three different MC generators are used to compare the predictions of the distributions of several observables. The $2 \to 2$ as well as the $2 \to 3$ production modes, as described in Section 2.3.1, are implemented in the MC generators. The differences of both schemes are compared, as well as the MC event generators AcerMC and Powheg. Finally, radiative corrections in the top-quark decay are studied.

Figure 5.1 shows the Feynman diagram of the $2 \to 3$ single top-quark t-channel production, including the top-quark decay. The full event signature incorporates three quarks, one forward light-quark jet, two b-quark jets, one originating from the initial gluon splitting and the other one from the top-quark decay. As already discussed in Section 2.3.1, the final state b quark emerging from the initial gluon splitting, is called $2^{\rm nd}$ b quark. Only the leptonic decay of the W boson is taken into account, since the signal-to-background ratio is superior to the hadronic decays that would include large multijet backgrounds. The leptons emerging from the W-boson decay can be an electron, a muon or a tau plus the corresponding neutrino. The neutrino itself cannot be observed by the ATLAS detector, but can be reconstructed measuring the missing transverse momentum.

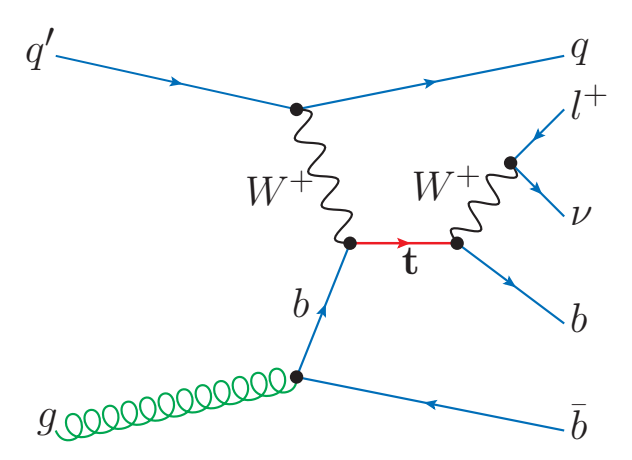


Figure 5.1: The final state signature of the $2 \to 3$ t-channel production. The full event signature includes one forward light-quark jet, two b jets, one originating from the initial gluon splitting and the other one from the top-quark decay. Only the leptonic decay of the W boson is taken into account.

5.1 Comparison of AcerMC and Powheg MC Generators

In this Section, the modeling of various kinematic distributions of the single top-quark t-channel are compared between AcerMC and Powheg, both generators are interfaced to Pythia. Powheg provides a MC event generation of the single top-quark t-channel $2 \to 2$ process at NLO accuracy, while AcerMC provides only partial NLO accuracy. AcerMC uses for the event generation of the single top-quark t-channel processes a combination of the already mentioned four- and five-flavour schemes. AcerMC therefore considers the $2 \to 2$ LO process (cf. Figure 2.3(a)) and adds the $2 \to 3$ NLO correction (cf. Figure 2.4(a)). The inclusion of the $2 \to 3$ NLO correction can result in a collinear singularity within the theoretical calculation, stemming from the initial gluon splitting into a $b\bar{b}$ -pair. AcerMC subtracts the collinear region, thereby removing the associated singularities. The ACOT mechanism [34, 35] provide a method of incorporating massive quarks into the factorisation theorem.

In order to precisely define the light quark in events produced by POWHEG, stemming from the initial quark radiating a W boson, real NLO corrections, have to be correctly associated to the light quark in the final state. POWHEG, might correct the light quark via final state gluon radiation, which decreases the energy of the light quark. The radiated gluon and the light quark are merged if their respective distance is below $\Delta R < 0.4$. The resulting object is called "light quark corrected". Since AcerMC only models that observable at LO precision, final state gluon radiation

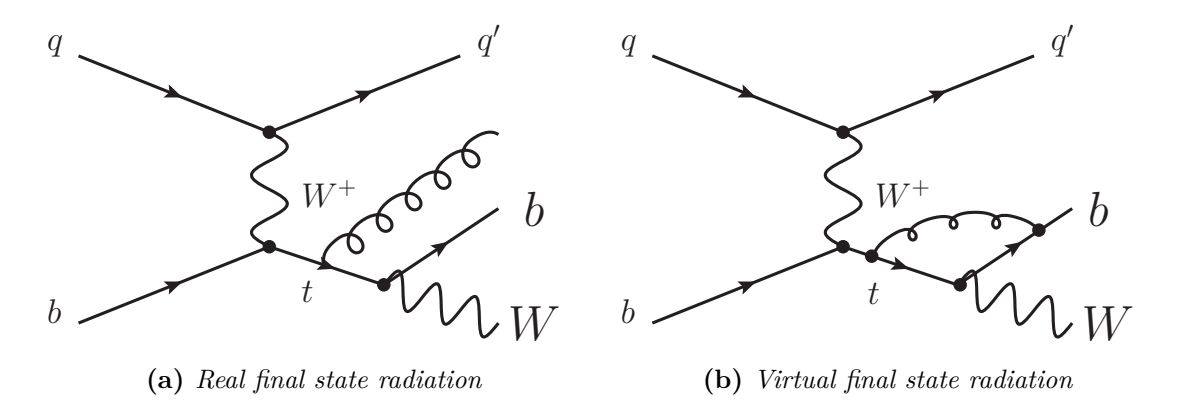


Figure 5.2: Examples for real and virtual next-to-leading-order corrections.

does not enter the calculation, thus leaving no ambiguities within the light quark definition.

Figure 5.3 and Figure 5.4 illustrate the modeling of the η and $p_{\rm T}$ distributions for various observables obtained from both MC generators. In general we observe a very good agreement between the studied generators. Only small differences have been found in the distribution of the light quark η , shown in Figure 5.4(c), which is broader for Powheg compared to AcerMC and the $p_{\rm T}$ distribution, Figure 5.4(d), is softer for Powheg than AcerMC. The differences can be explained with the NLO corrections, which are only applied for Powheg. The corresponding distributions are not compared for the $2^{\rm nd}$ b quark since no unambiguous definition of this parton could be found for the Powheg generator.

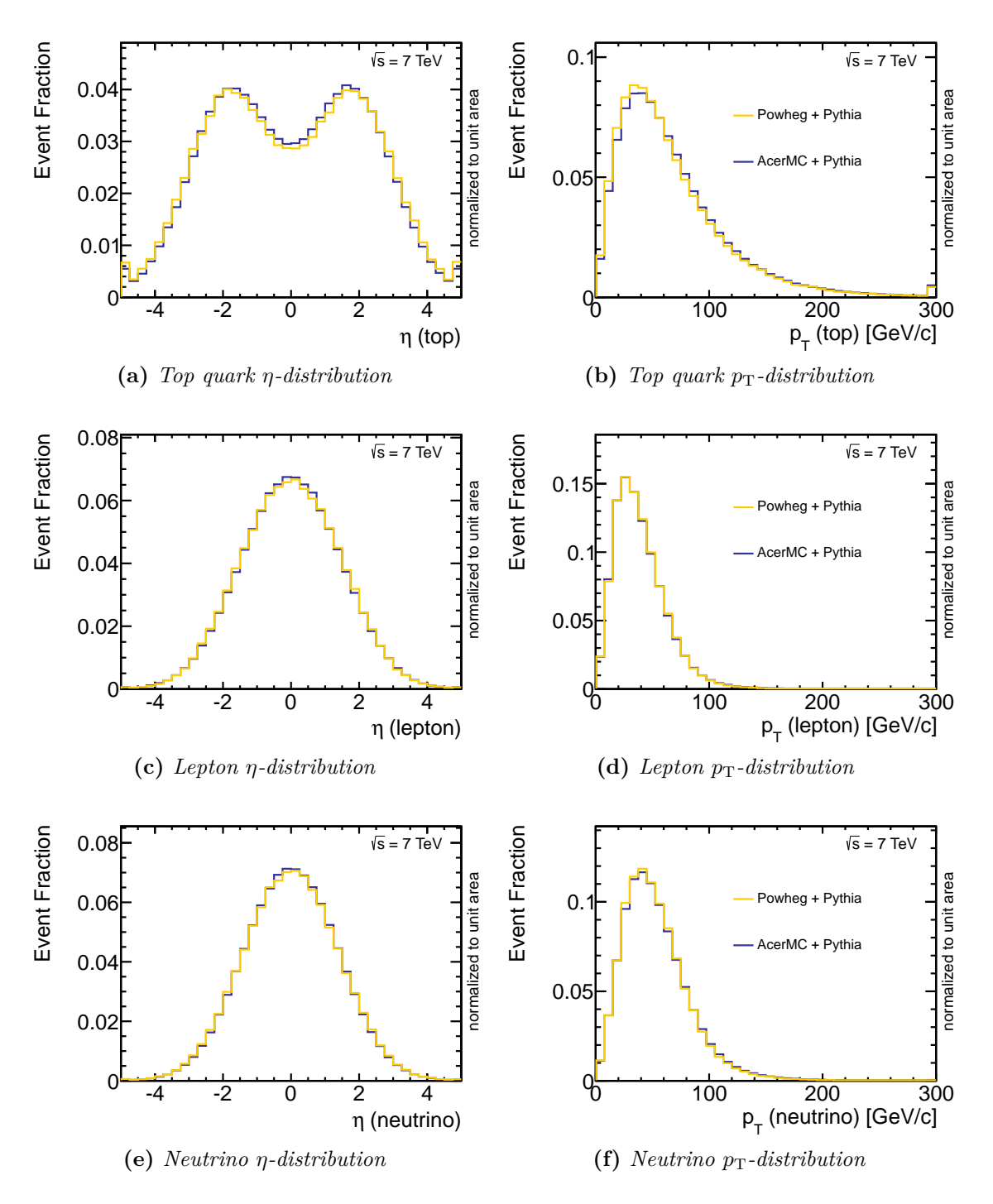


Figure 5.3: η - and p_{T} -distributions of various observables, for AcerMC and Powheg. The agreement of AcerMC and Powheg in these variables is very good.

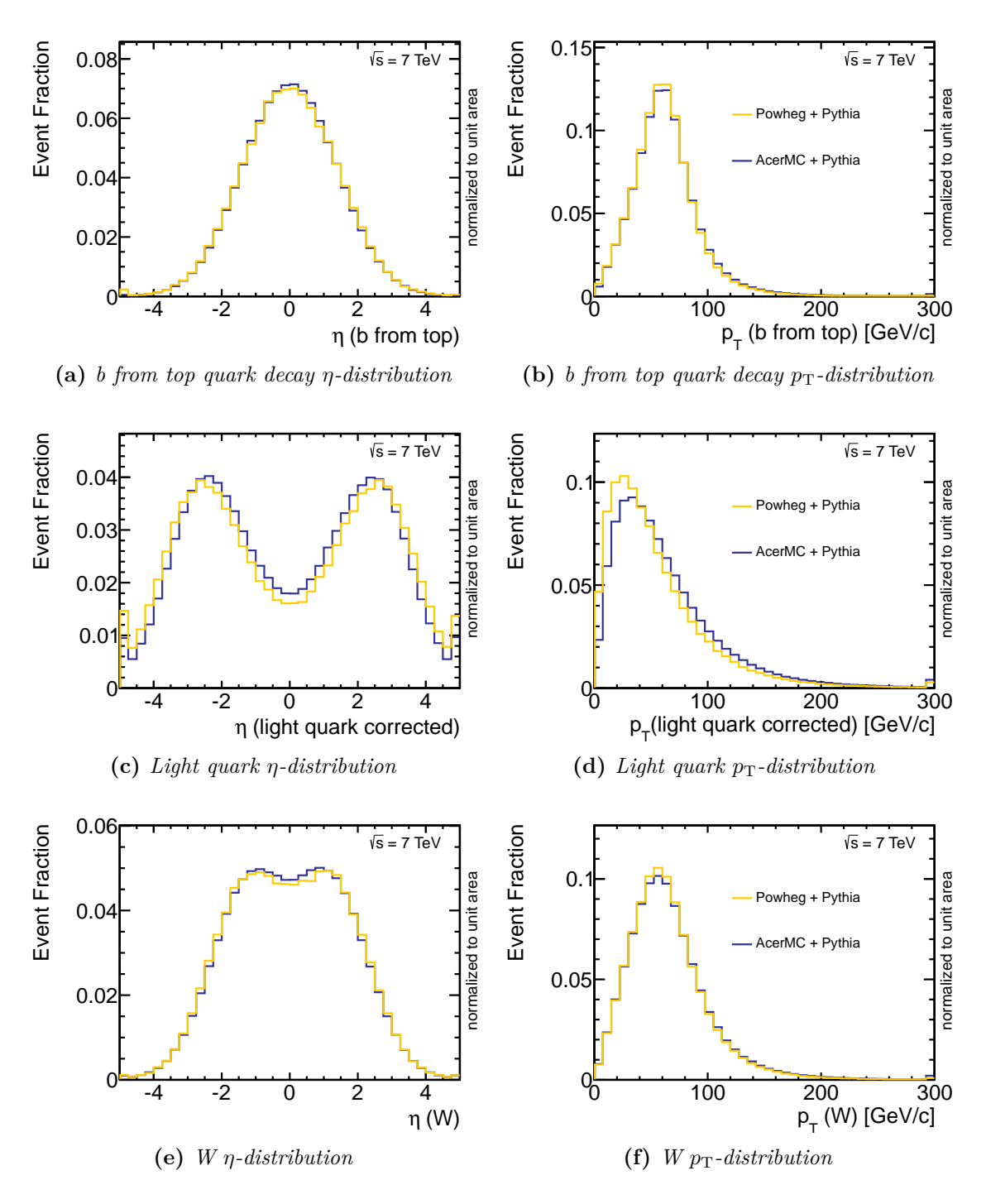


Figure 5.4: η - and p_{T} -distributions of various observables, for AcerMC and Powheg. The agreement of AcerMC and Powheg in these variables is very good. Small differences in c) and d) can be explained with the NLO corrections, which are only applied in Powheg.

5.2 Evaluation of MCFM Parton Level Simulation

The Monte Carlo for FeMtobarn processes (MCFM) [36] is a software for parton-level event integration at NLO accuracy for several important processes. It provides results for a series of processes especially including those containing the bosons W, Z and the Higgs boson, as well as heavy quarks. In the calculation of the single top-quark t-channel, MCFM is only considering the on-shell top quark production. When including NLO corrections for the single top-quark t-channel, it is possible to enable and disable the NLO contributions in the top-quark decay and only add initial-state and final-state radiation to the process at LO. In this Section the influence on the radiative corrections of the top-quark in the decay stage will be investigated [36].

In addition to single top-quark t-channel simulations provided by AcerMC and Powheg, MCFM simulation of the $2 \to 2$ (MCFM process number: 161,166) and $2 \to 3$ (MCFM process number: 233,238) single top-quark t-channel processes are evaluated at NLO accuracy. In this Section the MCFM $2 \to 2$ process is compared with Powheg, as well as the MFCM $2 \to 3$ process to AcerMC. The simulation is conducted using following selection cuts:

- Jet $p_{\rm T} > 15~{\rm GeV}$
- Jet $|\eta| < 6.0$
- $b \text{ jet } p_{\text{T}} > 15 \text{ GeV}$
- $b \text{ jet } |\eta| < 2.0$
- Lepton $p_{\rm T} > 20~{\rm GeV}$
- Anti k_T with $\Delta R = 0.4$

For all different processes the renormalisation and factorisation scales are given in Table 5.1.

Table 5.1: Renormalisation and factorisation scale for all generated processes with MCFM.

The calculated cross sections are given for top-quark and top-antiquark.

Process	Ren. scale	Fac. scale	Calculated cro	ss-section [fb]
$ \begin{array}{c} 2 \to 2 \text{ NLO} \\ 2 \to 3 \text{ NLO} \end{array} $	120	120 40	20491 ± 235 8946 ± 834	40410 ± 401 10422 ± 1152
$2 \rightarrow 3$ NLO + rad. corr. $2 \rightarrow 3$ NLO + rad. corr. $2 \rightarrow 3$ NLO + rad. corr.	172 40	172 40	225 ± 42 2048 ± 16	1745 ± 159 3948 ± 39

5.2.1 MCFM $2 \rightarrow 2$ NLO process versus Powheg

In this Section the POWHEG generator is compared to MCFM $2 \rightarrow 2$ NLO. At parton level both generators should yield similar results, since the calculation is based in both cases on the single top-quark t-channel $2 \rightarrow 2$ NLO process, but POWHEG is connected with the parton shower unlike MCFM. Top-quark, light-quark and b-quark η - and p_T -distributions, for MCFM $2 \rightarrow 2$ and Powheg are shown in Figure 5.5. The η distribution of the b quark, Figure 5.5(f), is broader for MCFM and more central distribution in case of the light quark, Figure 5.5(c). MCFM yields a harder light quark p_T distribution, Figure 5.5(d), compared to Powheg. The η distribution, Figure 5.5(a), for the top-quark is more forward than that of Powheg and the p_T , Figure 5.5(b), distribution is harder for MCFM. In case of the b-quark p_T distribution, Figure 5.5(f), both generators are in agreement.

In conclusion, both MCFM 2 \rightarrow 2 NLO and POWHEG yield significantly different result for most presented observables. The disagreement within the $p_{\rm T}$ distributions is due to the fact, that MCFM does not include parton shower simulation.

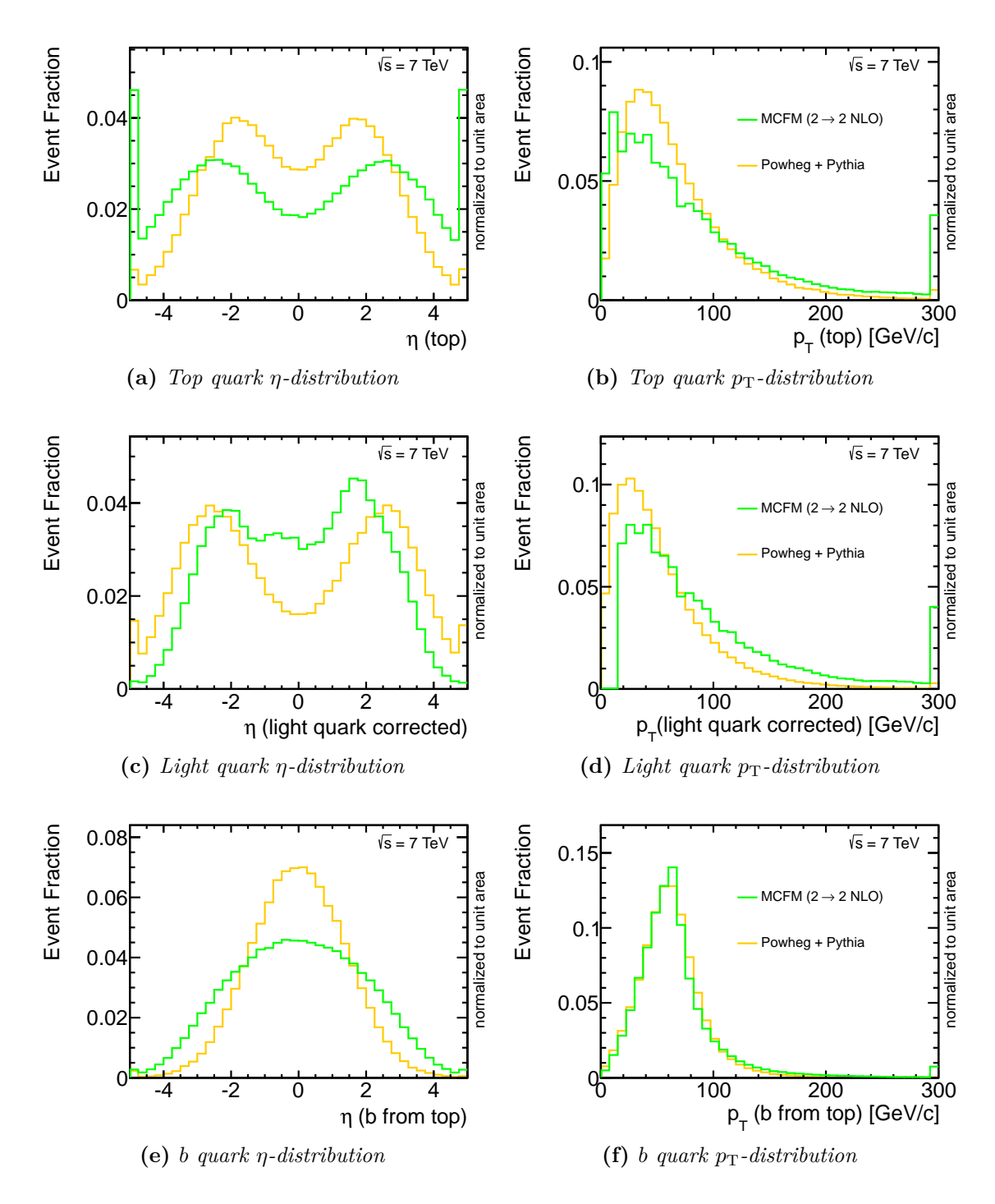


Figure 5.5: Top-quark, light-quark and b-quark η - and $p_{\rm T}$ -distributions, for MCFM $2 \to 2$ and Powheg. The η distribution of the b quark is broader for MCFM and more central distribution in case of the light quark. MCFM yields a harder light quark $p_{\rm T}$ distribution compared to Powheg. The η distribution for the top-quark is more forward than that of Powheg and the $p_{\rm T}$ distribution is harder for MCFM.

5.2.2 MCFM $2 \rightarrow 3$ NLO process versus AcerMC

MCFM $2 \to 3$ NLO is compared to AcerMC. The η distribution of the b quark is similar for MCFM compared to AcerMC (cf. Figure 5.6(e)). MCFM yields central distribution in case of the light quark, cf. Figure 5.6(c). MCFM yields a softer light quark $p_{\rm T}$ distribution compared to AcerMC, see Figure 5.6(d), and a harder b-quark $p_{\rm T}$ -distribution, cf. Figure 5.6(f). The η distribution, Figure 5.6(a), of the top quark is more central for MCFM compared to AcerMC and the $p_{\rm T}$ -distribution, Figure 5.6(b), harder for MCFM.

In conclusion AcerMC and MCFM $2 \rightarrow 3$ NLO yield more similar results than MCFM $2 \rightarrow 2$ NLO and POWHEG, but all presented $p_{\rm T}$ distributions differ between both generators which can be explained by the lack of shower simulation of the MCFM generator. AcerMC and MCFM $2 \rightarrow 3$ NLO are in substantial disagreement about the η distribution of the light quark, which is most probable due to a unclear definition of the light quark. Further studies are required to investigate that effect.

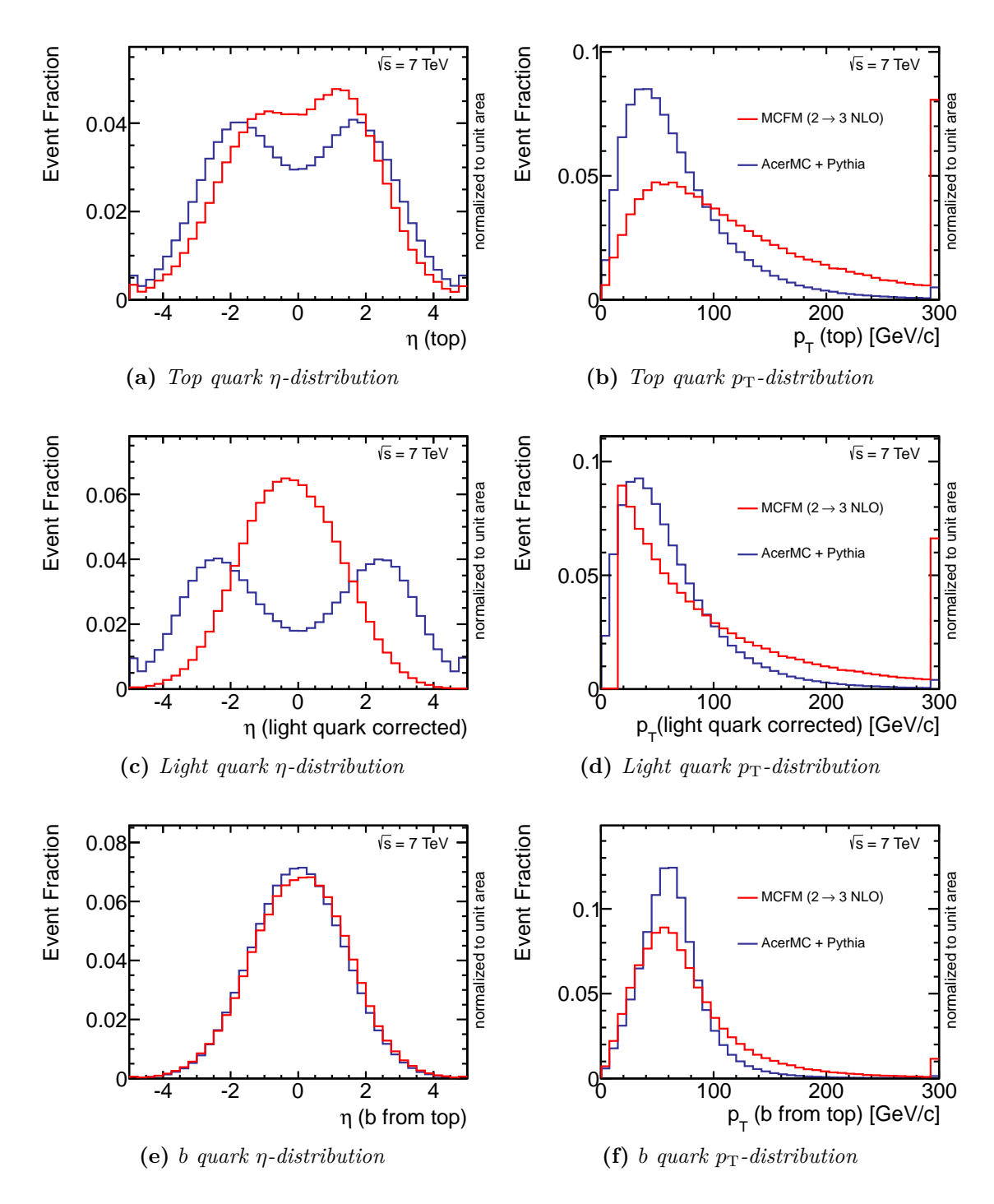


Figure 5.6: Top-quark, light-quark and b-quark η - and $p_{\rm T}$ -distributions, for MCFM $2 \to 3$ and AcerMC. The η distribution of the b quark is similar for MCFM compared to AcerMC and MCFM yields central distribution in case of the light quark. MCFM yields a softer light quark $p_{\rm T}$ distribution compared to AcerMC and a harder b-quark $p_{\rm T}$ -distribution. The η distribution of the top quark is more central for MCFM compared to AcerMC and the $p_{\rm T}$ -distribution harder for MCFM.

5.2.3 Evaluation of radiative corrections in the top-quark decay

In this section the influence of the inclusion of radiative effects in the top-quark decay is evaluated. In Reference [37] the production of the single top-quark including the top-quark decay have been presented at NLO accuracy. Radiative effects have been included both in the production stage and the decay stage of the top-quark, in contrast to the studies conducted in the previous sections. The calculation gives a good treatment of the jet activity associated with single top-quark production. Both the virtual and real contributions of the final state top-quark decay stage have been taken into account. The MCFM program provides the calculation for either the inclusion of the radiative effects at the decay stage or not.

Figure 5.7 illustrates the impact of the radiative corrections in the decay of the top quark. For the top quark and W boson η - and $p_{\rm T}$ -distributions, for MCFM $2 \to 2$ and MCFM $2 \to 2$ with radiative corrections in the decay stage of the top quark (t dec), are presented. The top-quark η -distribution, Figure 5.7(a), becomes more central when the radiative corrections are included in the top-quark decay and the $p_{\rm T}$ distribution gets softer, Figure 5.7(b). The η - and $p_{\rm T}$ -distributions of the W boson are not significantly altered, due to that correction, cf. Figure 5.7(c) and Figure 5.7(d). In conclusion, the corrections alter only the η - and $p_{\rm T}$ -distributions of the top-quark in a significant manner.

In this chapter two MC event generators have been compared with respect to various kinematic distributions. In Section 5.1 the event generators AcerMC and POWHEG have been compared, yielding an overall similar behaviour in nearly all observables presented. The only exception is the modeling of the final state light quark, in both η and $p_{\rm T}$, probably due to ambiguities in the reconstruction. Section 5.2 contains the evaluation of MCFM generated events in comparison with AcerMC and POWHEG. The studies conducted in this Section yield, that the modeling of the single top-quark t-channel with MCFM, using the four and five flavour schemes, is similar to both AcerMC and POWHEG in various observables. Certain attributes, especially the $p_{\rm T}$ distribution of most particles, deviate from those predicted by the MC event generators. In case of the $p_{\rm T}$ distribution, this is due to lack of a shower simulation within the MCFM generator.

Within the scope of this Thesis, further studies to understand differences between the NLO calculation and the implementation of the MC generators could not be conducted. Especially studies of the choice of the renormalization and factorisation scales, the PDF choice or cuts on the partons would be interesting subjects.

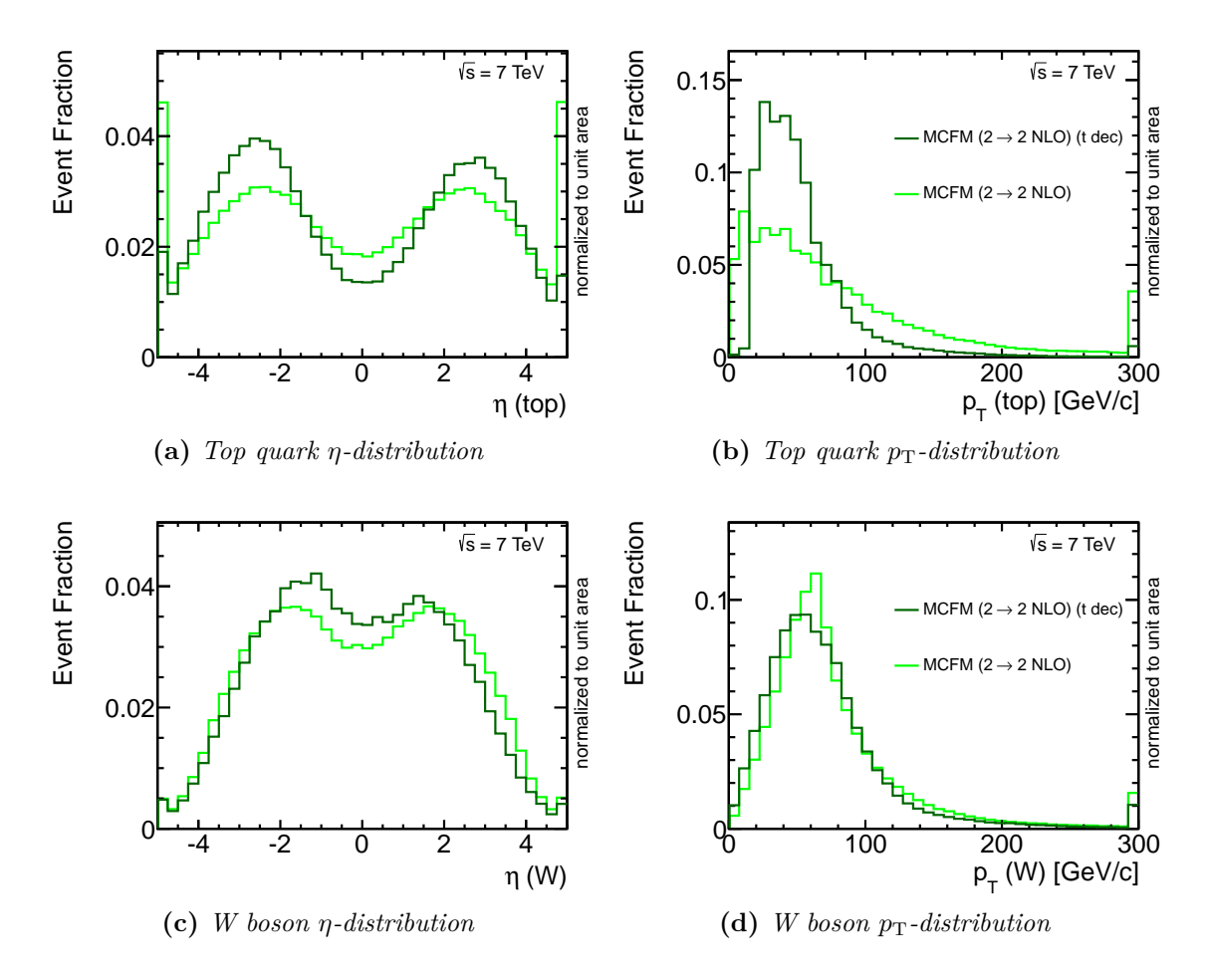


Figure 5.7: Top quark and W boson η - and p_T -distributions, for MCFM $2 \to 2$ and MCFM $2 \to 2$ with radiative corrections in the decay stage of the top quark (t dec). The top-quark η -distribution becomes more distinct when the radiative corrections are included in the top-quark decay and the p_T distribution gets softer. The η - and p_T -distributions of the W boson are not significantly altered, due to that correction.

6 Object Reconstruction

Based on the measured data of the ATLAS detector, objects can be defined as a composition of the provided data.

6.1 Charged Track Reconstruction

Charged tracks, can be reconstructed using the data measured by the Inner Detector, but due to the high number of produced particles resulting in a high amount of hits in all layers of the ID, a reconstruction is difficult. In ATLAS two sequential track reconstruction approaches are used. A more detailed description of the ATLAS track reconstruction algorithms are presented in [38]. The inside-out track reconstruction is the first presented search strategy. The pattern recognition of the ID is initially seeded in the inner silicon tracker and performs a hit finding towards the outer border of the ID. At first, the inside-out track reconstruction creates three-dimensional representations of the measurements obtained with the silicon detector. Than track seeds are built which lead to track candidates by applying a window search given by a seed direction. Different measured hits in the extrapolated search path, are assessed towards their compatibility with the evaluated track, with a simplified Kalman filter [39].

The second track reconstruction strategy is the outside-in sequence. The necessity for the second strategy, is stemming from the fact, that not all tracks can be found by the inside-out sequence. Ambiguous hits can lead to the refusal of a track if the track seed has been shadowed which is an electronic artifact, leading to a fake measured hit. In addition, objects like displaced tracks may not have hits in the innermost ID layer and would therefore be missed by that strategy.

The outside-in sequence is reverse to the inside-out sequence and therefore is initiated with track seeds in the outermost part of the ID, the TRT. The pattern recognition uses an association tool to prevent the usage of hits that have already been assigned by the inside-out sequence.

An average track has 3 pixel hits, 4 space-points in the SCT and about 36 hits in the TRT. The intrinsic measurement accuracy has been described in section 3.2.2, leading to efficient track recognition within $|\eta| < 2.5$ and down to $p_{\rm T} \approx 500$ MeV.

6.2 Vertex Reconstruction

The purpose of vertex reconstruction is the identification of common intersections of multiple tracks. The vertex reconstruction enables to differentiate the proton-proton collision, called primary vertex, from decays of unstable particles produced in the collision. The reconstruction relies strongly on the track reconstruction. Primary vertices are reconstructed with an iterative vertex finding algorithm [40]. The primary vertex is seeded from the z-position at the beamline of the reconstructed tracks. The compatibility, with a primary vertex, of tracks in the vicinity is tested with a χ^2 fit. The resulting weight of each track is a measure of this compatibility. If a track is found, with a displacement, beyond a 7σ environment of the primary vertex, it seeds a new vertex. This procedure is repeated until no additional vertices can be found. A reconstructed vertex is required to have two tracks, but for robustness, three tracks can be required. The efficiency to reconstruct a vertex from a minimum bias interaction, as a function of the average number of interaction per bunch crossing, is shown in Figure 6.1(a). As the average number of interactions per bunch crossing rises, the reconstruction efficiency decreases, reaching ≈ 50 % at $\mu = 41.$

The rising number of fake tracks, due to pile-up, increases the probability to reconstruct a fake vertex (cf. Figure 6.1(b)). When applying the robust criteria to the vertex (i.e. requires at least three tracks), the fake vertex reconstruction probability drops significantly. [41]

6.3 Charged Lepton Identification

Initially an electron is reconstructed by a seeding cluster of transverse energy which has been measured in the electromagnetic calorimeter. The seeding cluster must exceed a transverse energy threshold of $E_{\rm T}>2.5$ GeV. Of all previously reconstructed tracks, one is selected which yields the highest compatibility with an extrapolated flight-path of an electron, to the seeding cluster. The transverse energy measured in the calorimeter and the transverse momentum obtained from the track reconstruction, are associated to the found electron.

Tracker and calorimeter information are used to define three classes of electron identification. These consecutive sets of requirements are called "loose", "medium" and "tight". Each class contains the requirements of the inferior class and adds constrains which lead to a higher electron probability. More details on the identification requirements can be looked up in [42, 43].

The muon identification and reconstruction in ATLAS is incorporating the measured hits of the subdetectors introduced in Section 3.2.4. The used algorithms provide three different reconstruction approaches. These algorithms rely on different

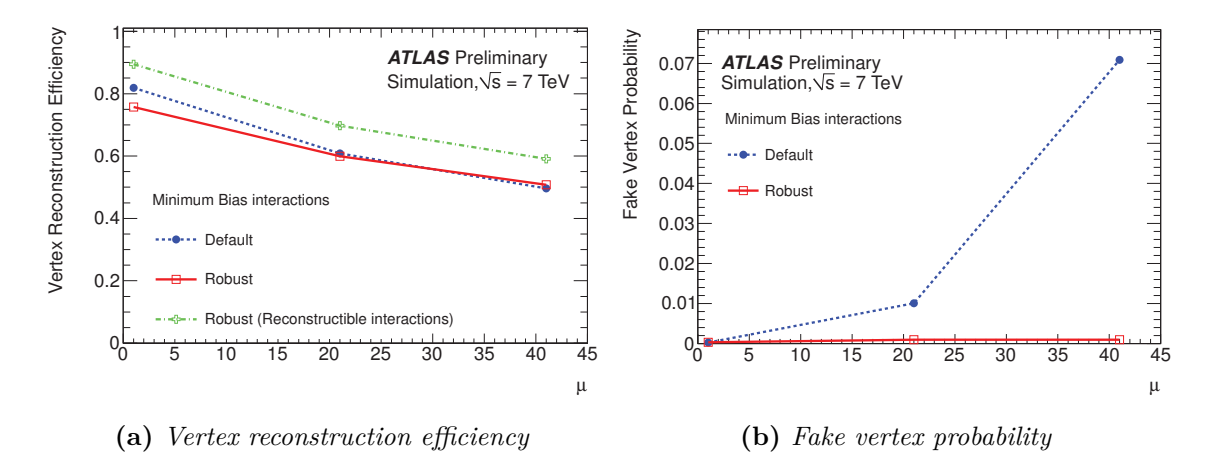


Figure 6.1: The vertex reconstruction efficiency (a) and fake probability (b) as a function of the average number of interactions in minimum bias Monte Carlo simulation. These are shown both using default track selection (blue, dashed) and with the robust track requirements (red, solid). The vertex reconstruction efficiency with the robust track requirements is shown for reconstructible interactions (green, dot-dashed), defined as having at least two stable charged primary particles with $|\eta| < 2.5$ and $p_{\rm T} > 400$ MeV. [41]

parts of the ATLAS detector. The "standalone muon" reconstruction incorporated only information provided by the muon system whereas the "combined muon" and the "staco muons" additionally exploit information from the Inner Detector. Additional information can be found in [44].

6.4 Jet Reconstruction

The ATLAS jet reconstruction provides multiple reconstruction algorithms. The first type are cone jet algorithms, which attempt to mimic the clustered energy depositions measured by the calorimeter with cones and the second type are topological algorithms, or $k_{\rm T}$ algorithms, which consider the topological substructure of a jet. The anti- $k_{\rm T}$ algorithm [45] is the default ATLAS jet finder and is used with the FASTJET implementation of this algorithm.

 $k_{\rm T}$ algorithms introduce the distance d_{ij} between the clusters i and j, as well as the distance d_{iB} between cluster i and the beam B:

$$\begin{aligned} d_{ij} &= & \min \left(p_{\mathrm{T}_i}^{2m}, p_{\mathrm{T}_j}^{2m} \right) \frac{(\Delta R)_{ij}^2}{R^2}, \\ d_{iB} &= & p_{\mathrm{T}_i}^{2m}, \end{aligned}$$

where the m parameter distinguishes between different algorithms, $(\Delta R)_{ij}^2$ is the distance between cluster i and j in the η - ϕ plane. R is the resolution capability with respect to the beam.

The anti- $k_{\rm T}$ algorithm works with sequential recombination of soft and hard particles. If two particles are close to each other, in terms of the introduced distance weight, they are recombined into a new object, with respect to their four vectors. The algorithm tends to cluster soft particles with hard ones, before they cluster with other soft particles. The procedure is recursively repeated until the separation, and therefore the distance, of all objects exceeds a preset value. After the anti- $k_{\rm T}$ algorithm is applied, ideally all objects are clustered into jets.

6.5 Missing Transverse Momentum

Neutrinos cannot be directly measured by the ATLAS detector itself, but must be reconstructed. Every particle that is produced in the primary interaction and all subsequent particles, should have no transverse momentum in total, since the colliding protons carry only longitudinal momentum. If the total transverse momentum is not completely balanced the discrepancy is called missing transverse momentum $\not\!\!E_T$. This $\not\!\!E_T$ is the only indication of the presence of a neutrino in an event. The $\not\!\!E_T$ is defined as:

$$\cancel{E}_{\rm T} = \sqrt{(E_x^{\rm miss})^2 + (E_y^{\rm miss})^2}$$
with
$$E_{x,y}^{\rm miss} = E_{x,y}^{\rm miss,calo} + E_{x,y}^{\rm miss,\mu}$$
(6.1)

The calorimeter term is defined as:

$$E_x^{\text{miss,calo}} = -\sum_i^{N_{\text{cell}}} E_i \sin \theta_i \cos \phi_i$$
 and
$$E_y^{\text{miss,calo}} = -\sum_i^{N_{\text{cell}}} E_i \sin \theta_i \sin \phi_i$$

where E_i , θ_i and ϕ_i are the energy, the polar angle and the azimuthal angle of the calorimeter cell. The muon contribution $E_{x,y}^{\text{miss},\mu}$ is obtained from the momenta of muon tracks reconstructed within a pseudorapidity of $|\eta| < 2.7$:

$$E_{x,y}^{\mathrm{miss},\mu} = \sum_{\mathrm{muons}} \overrightarrow{p}_{x,y}$$

7 b-tagging

The identification capability of a b-quark jet is crucial for most physics processes which will be investigated at the LHC, as it is a key ingredient to efficiently select the desired signal events from a very high number of background events. The importance of the b-quark is stemming from the fact that, the top-quark is almost exclusively decaying into a bottom-quark, as discussed in section 2.2. There are several physical features of the b-quark, which lead to the capability to distinguish b-quark jets from light quark jets. When a b-quark is produced, it hadronises into a b-Hadron. The average lifetime of a b-Meson is $\tau = 1.57$ ps [6], b-baryons have a similar lifetime. Considering the fact, that the b-quark and subsequently the b-hadron carry a large boost, leads to the fact that the flight path of a b-hadron has in average a measureable offset from the primary vertex of the b-hadron has in average a measureable offset from the primary vertex. Hence the decay vertex is called secondary vertex. The impact parameter d_0 is the closest distance of approach of the particle trajectory to the beam line.

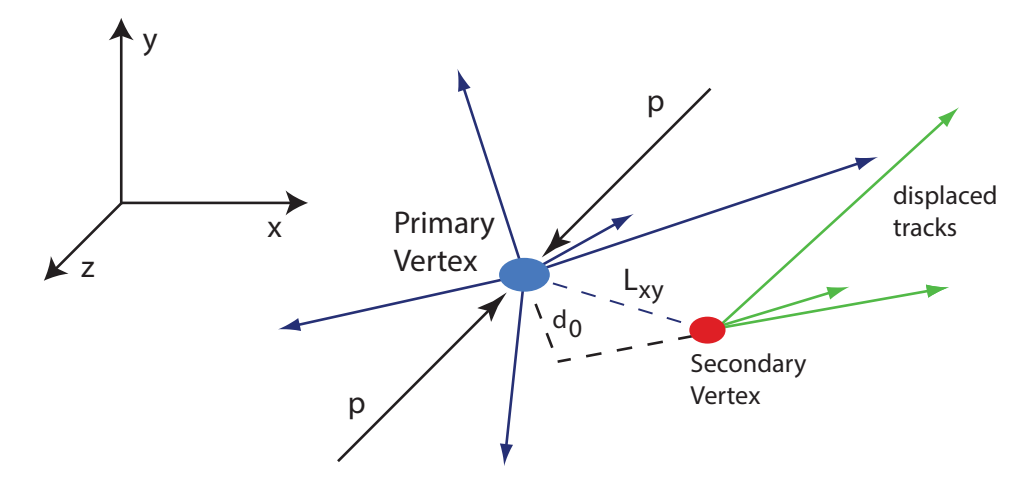


Figure 7.1: Schematic view of displaced tracks with impact parameter d_0 forming a secondary vertex. L_{xy} is defined as the projection of the two-dimensional decay length on the jet axis.

Figure 7.1 gives a schematic of a secondary vertex. The displaced tracks can not be traced back to the primary vertex, but are consistent with a second vertex.

7 b-Tagging

Prior to the utilisation of a b-tagging algorithm in a physics analysis, the performance has to be validated with collision data. Monte Carlo simulations cannot perfectly describe the performance of the detector [46]. The b-tagging calibration yields scale factors for the correction of rate differences between MC and data.

7.1 Baseline Track Selection

By design, well-measured tracks are utilised for b-tagging to reject fake tracks and those from long-lived particles (K_s , Λ or other hyperon decays) and material interactions (photon conversions or hadronic interactions). Two different quality levels are defined to suppress background tracks. The standard quality requires minimal seven precision hits, while the b-tagging quality in addition requires two hits in the pixel detector, from which one must be in the b-layer of the Pixel Detector. The transverse and longitudinal impact parameters at the perigee must fulfill $|d_0| < 2$ mm and $|z_0 - z_{\rm pv}| \sin \Theta < 10$ mm respectively, where z_{pv} is the location of the primary vertex. The transverse momentum threshold for all tracks is $p_{\rm T} > 1$ GeV. Additionally the b-tagging quality requires $|d_0| < 1$ mm and $|z_0 - z_{\rm pv}| \sin \Theta < 1.5$ mm. The b-tagging quality selection criteria are used by all tagging algorithms which are relying on the impact parameter of tracks. Secondary vertex algorithms use looser selection criteria.

7.2 b-tagging Algorithms

A variety of tagging algorithms has been developed to identify b-quark jets.

7.2.1 Impact parameter tagging algorithms

The first family of b-tagging algorithms are the impact parameter tagging algorithms. They rely on the signed impact parameter, to discriminate the tracks from a b-hadron decay, against tracks stemming from the primary vertex. The sign is based on the assumption, that the decay point of the b-hadron must lie along its flight path. The sign of the impact parameter is defined as:

$$\operatorname{sign}(d_0) = \operatorname{sign}\left(\left(\vec{P}_j \times \vec{P}_t\right) \cdot \left(\vec{P}_t \times \left(\vec{X}_{pv} - \vec{X}_t\right)\right)\right),\tag{7.1}$$

where \vec{P}_j is the jet direction as measured by the calorimeters, the direction \vec{P}_t and the position \vec{X}_t of the track at the point of closest approach to the primary vertex and the position \vec{X}_{pv} of the primary vertex.

The distribution of the signed transverse impact parameter d_0 is shown on Figure 7.2, Figure 7.2(a), for tracks coming from b-quark jets, c-quark jets and light-quark jets. Figure 7.2(b) shows the significance distribution d_0/σ_{d_0} which gives more weight to precisely measured tracks. The impact parameter significance is defined as d_0/σ_{d_0} , where σ_{d_0} gives the uncertainty of the measurement of d_0 .

Tracks from b/c- hadron decays tend to have a positive sign, while the sign of prompt tracks from the primary vertex is random. The combination of the impact parameter significances, both longitudinal and transverse, are the foundation for the three tagging algorithms: IP1D relies on the longitudinal impact parameter, IP2D on the transverse impact parameter and finally IP3D which uses two-dimensional histograms of the longitudinal versus transverse impact parameters, taking advantage of their correlations. [46]

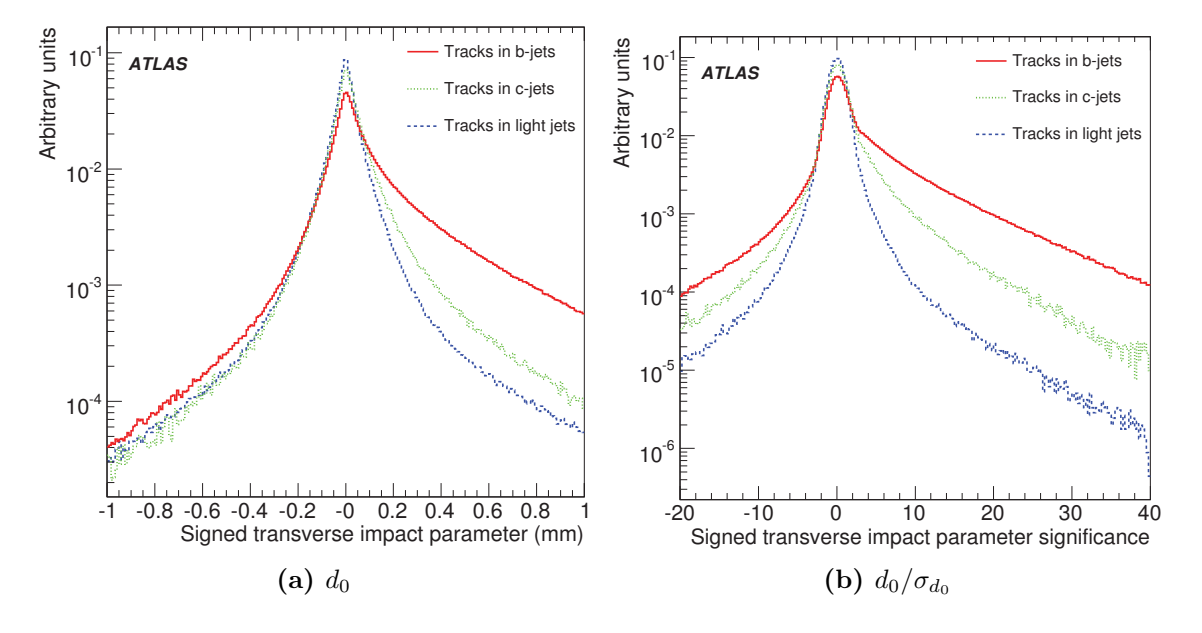


Figure 7.2: Signed transverse impact parameter d_0 distribution, Figure 7.2(a) and signed transverse impact parameter significance d_0/σ_{d_0} distribution, Figure 7.2(b), for b-quark jets, c-quark jets and light quark jets [41].

7 b-Tagging

7.2.2 Secondary vertex tagging algorithms

To improve the discrimination power of impact parameter tagging algorithms between b-quark jets and light jets, the inclusive reconstruction of the secondary vertex is considered. Under the premise, that a viable vertex has been reconstructed, three vertex properties are exploited: the number of tracks vertices, the ratio of the sum of the energies of the vertex tracks to the sum of the energies of all tracks in the jet, and the invariant mass of all tracks associated to the vertex. The so-called SV tagging algorithms are relying differently on these properties.

The JetFitter exploits the topological structure of b- and c-hadron decays. A Kalman filter is used to locate a common line on which the primary vertex, the bottom vertex, as well as the charm vertex, are located. The b-hadron approximate flight path is obtained from the position of the c,b vertices on the previous found line. Even if only a single track could be reconstructed for each corb vertex, this method will not merge the vertices. As a result of the tagging algorithm, a likelihood is provided to discriminate the c-jets, b-jets and light-jets.

7.2.3 Combining tagging algorithms

Even though different tagging algorithms can be combined, it has been done only for those based on likelihood ratios, since the formalism is easy. The combination of any number of taggers can be achieved through summing up the individual tagging weights.

7.2.4 JetFitterCOMBNN(c)

The so-called JetFitterCOMB is a combination of the secondary vertex tagging algorithm JetFitter and the impact parameter tagging algorithm IP3D. In addition the JetFitterCOMBNN (JF) uses Neural Network (NN) techniques to improve the separation of b-quark jets and light jets. The JetFitterCOMBNNc (JFc) variant uses a likelihood-ratio test, as the JF does, but is designed to suppress c-quark jets. The individual jet-flavour probability is denoted p_u (light-quark jet probability), p_b (bottom-quark jet probability) and p_c (charm-quark jet probability).

The weight of the JF b-tagger is obtained via $w \equiv \log(p_b/p_u)$, whereas JFc uses $w \equiv \log(p_b/p_c)$. The likelihood ratio test is a hypothesis test which yields a weight corresponding to the probability that an evaluated jet is likely to be a b-quark jet or of light/c flavour.

The ATLAS collaboration provides different calibrated working points for each b-tagger. The percentage gives the b-jet tagging efficiency and w is the corresponding minimum weight to be required in the discriminant distribution:

JetFitterCOMBNN

- 57%(w > 2.20)
- 60%(w > 1.80)
- 70%(w > 0.35)
- 80%(w > -1.25)

JetFitterCOMBNNc

- 50%(w > 1.33)
- 55%(w > 0.98)

7.2.5 MV1

The MV1 b-tagging algorithm is based on a neural network using the output weights of the JetFitter+IP3D, IP3D and SV1 algorithms as input.

The neural network is a perceptron with two hidden layers with respectively three and two nodes, leading to an output layer with a single node. The training of the network is done with two simulated samples of b- and light jets, from a mixture of $t\bar{t}$ events and higher- $p_{\rm T}$ dijet events. Since the tagging performance is very dependent on the $p_{\rm T}$ and, to a lesser extent, on the η of the jet, biases from the kinematic spectra of the training samples are avoided by using weighted events: each jet is assigned to a category defined by a coarse 2D grid in $(p_{\rm T}, \eta)$, its weight is defined according to the overall fraction of all jets in this category, and the jet category is fed to the network as an additional input variable. The output weight of the MV1 algorithm is shown in Figure 7.3, for b-jets, c-jets and light jets from simulated $t\bar{t}$ events. Heavy-flavour jets have preferably large weights compared to light jets. The spike around 0.15 corresponds mostly to jets for which no secondary vertex could be found [47].

The ATLAS working points for the MV1 b-tagger are as follows:

- 60%(w > 0.905363)
- 70%(w > 0.601713)
- 75%(w > 0.404219)
- 85%(w > 0.0714225)

7 b-Tagging

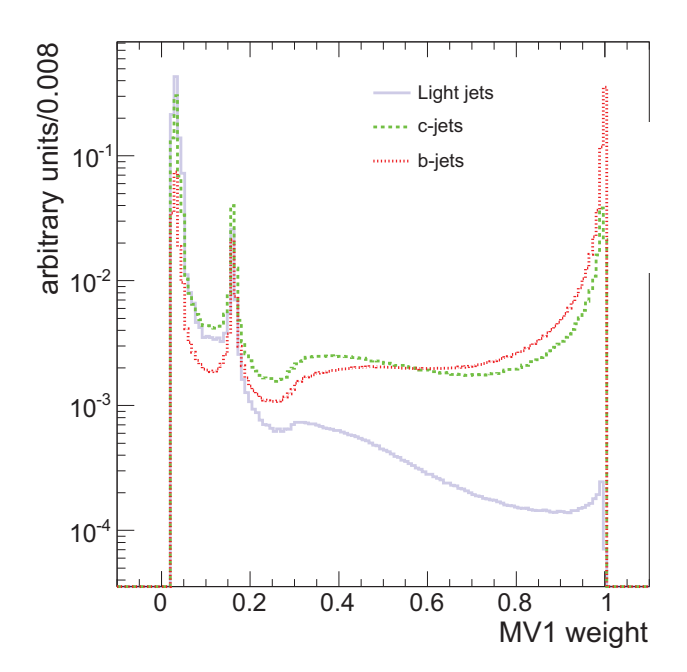


Figure 7.3: Distribution of the tagging weight obtained with the MV1 algorithm, for three different flavours of jets. The jets are obtained from a sample of simulated $t\bar{t}$ event . [47].

7.3 Studies on b-tagging Calibration

A b-tagging calibration yields scale factors for the correction of rate differences between MC and data. A b-tagging calibration is, in most cases, performed for various so called working points which are fixed for a preselected tagging efficiencies. Detailed information can be taken from Reference [46].

Preparation studies for a b-tagging calibration are conducted in this Section, for use in single top-quark analyses.

In order to get a pure b-quark sample a selection of $b\bar{b}$ events is developed. The tag-and-probe method is used to enrich the selected events in b-quark jet flavour. This method has the advantage, that requirements are applied only on one jet, the tag-jet, whereas the second jet is kept unbiased, the probe-jet. The criteria which a tag-jet has to fulfill are arising from the kinematic properties of the $b\bar{b}$ production and decay. Both b quarks are of equal mass and therefore the momenta are pointing in approximately opposite directions in the transverse plane. For the tag-jet, we consider the semi-leptonic b-hadron decay modes, which result in a lepton in the final state as well as one hadron. When taking the difference in mass from the b quark and the light quarks (u, d and s) into account, the emerging hadrons and the lepton, should have a considerable boost and therefore a small angular spread. All cuts that are applied to either the event or an object within a selected event are defined as follows:

- Events must contain at least two jets
- Minimum transverse lepton momentum of $p_T > 8 \text{ GeV}$
- Minimum transverse jet momentum of $p_T > 25 \text{ GeV}$
- Anti- $k_{\rm T}$ jet algorithm R=0.4
- Jet and lepton pseudorapidity of $|\eta| < 2.5$

In addition special objects need to be defined:

tag-jet The jet containing a lepton. The lepton must be found within $\Delta R < 0.4$ of the jet axis.

away-jet The jet pointing away from the tag-jet. The away-jet must have a $\Delta \phi > 2.0$ with respect to the corresponding tag-jet. If multiple away-jet candidates are available, the one yielding the lowest value $y = |\pi - \Delta \phi|$ is selected.

To obtain an enhanced unbiased sample of puark jets, only the tag-jet is required to include a lepton, while the away-jet is used fur further studies. To conduct the calibration studies Pythia dijet MC samples are used. The samples are subdivided according to the number of jets. Only the jet multiplicities one to five are considered in this study, see Section 4.1.3. The events in all MC samples are further grouped according the jet truth flavour. Since there are multiple jets in a selected event all flavours can occur. A prescription is defined as follows:

7 b-Tagging

- c-quark jets supersede all found light jets
- b-quark jets supersede all found c and light jets

In summary, an event classified as b-quark can contain c-quark or light-quark jets, which can be selected as tag-jet and away-jet in a multi jet event.

After the cuts are applied and $b\bar{b}$ candidate events are reconstructed from the introduced objects, a fraction fit determines with a maximum likelihood method the composition of all three jet flavours. The reconstructed secondary vertex mass distribution of the away-jet is used in the fit.

Figure 7.4(a) shows the distribution of the secondary vertex mass of the away-jet vertex in the pre-tagged sample, normalised to fit results. Pre-tagged means that no b-tagging requirements are included in the selection decision. All three jet flavour contributions are indicated by the different colours b flavour (blue), c flavour (green) and light flavour (red). Figure 7.4(b) shows the corresponding distributions normalised to unit area. In both cases the simulation models the collision data in an acceptable way. The deviation at lower values of the invariant mass distribution cannot be explained at the time, but might stem from a wrong modelling of light quark jets for very low vertex masses.

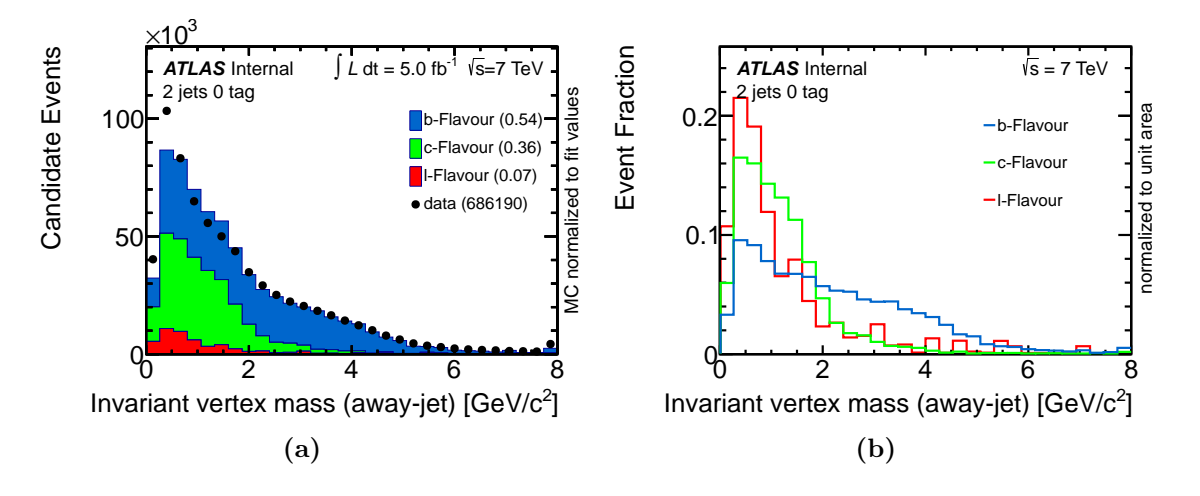


Figure 7.4: Secondary vertex mass distribution of the away-jet in the pre-tagged sample, normalized to fit results. The contributions from b flavour (blue), c flavour (green) and light flavour (red) are depicted, as well as the data (black). In the bracket the fitted flavour fraction of the respective process is given. Figure 7.4(b) depicts the corresponding distribution, normalised to unit area.

In order to further increase the fraction of b-quark jets, additional cuts on the tag-jet must be applied. To discriminate non-b-quark jets different b-taggers are used, since they, by design, comprise various variables to suppress c- and light-quark jets. As discussed in section 7, different b-taggers are used in ATLAS of which the

JF, JFc and MV1 tagging algorithms are being evaluated. In order to maximise the fraction of the b-quark jets in the sample, the working points with the highest purity are chosen. These working points feature 57% efficiency for the JF, 50% efficiency for the JFc and for the MV1 60% efficiency.

Figure 7.5 illustrates the impact of the three mentioned b-taggers. In Figure 7.5(a) the JF at 57% efficiency has been applied to the tag-jet and the resulting b-quark enhanced sample is drawn in the secondary vertex mass of the away-jet and the corresponding plots for the JFc and MV1 are shown in Figure 7.5(b) and 7.5(c) . A summary of the results is given in Table 7.1. MV1 is the recommended b-tagging algorithm, yields the lowest b flavour fraction, while the JF and especially the JFc provide a more stringent rejection of non-b-quark jets.

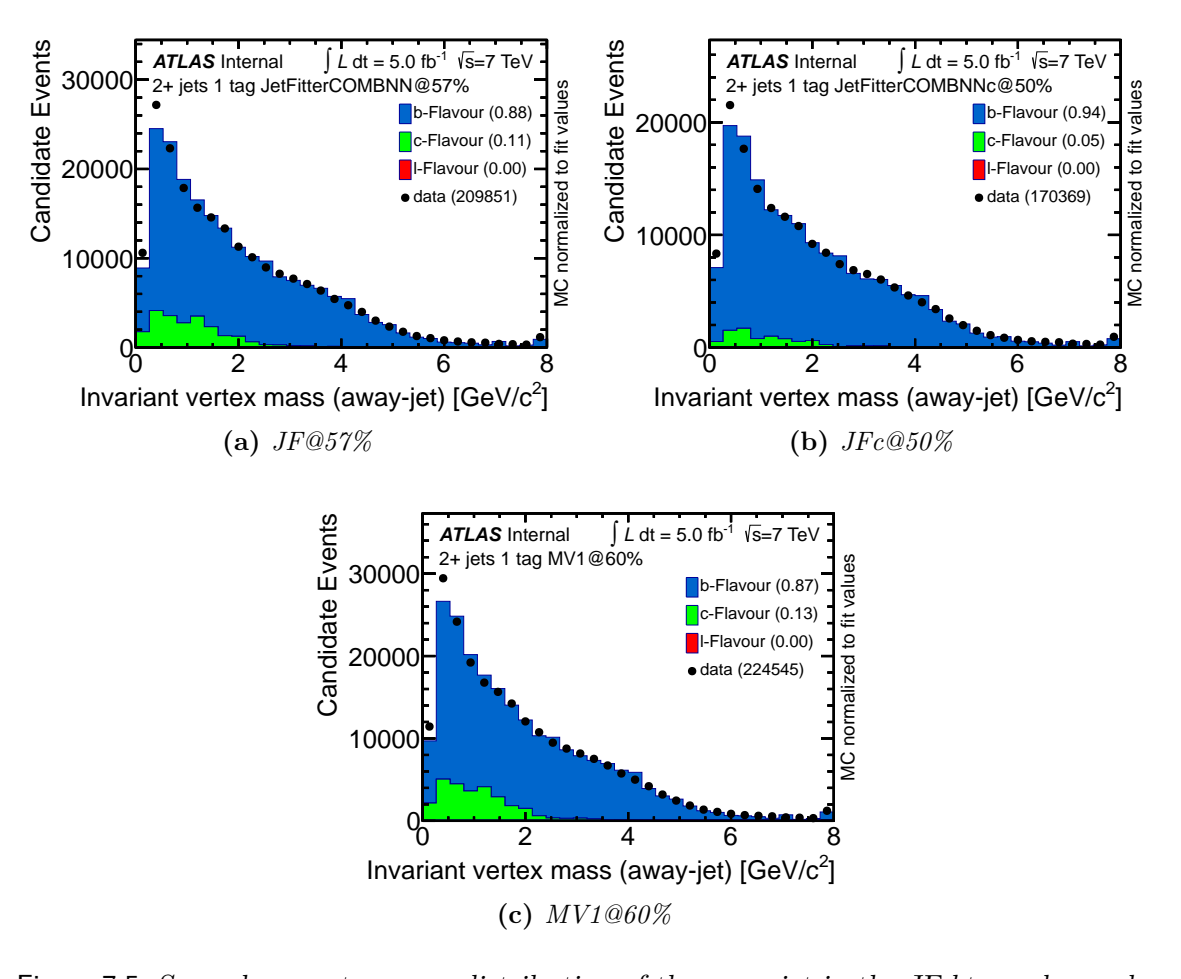


Figure 7.5: Secondary vertex mass distribution of the away-jet in the JF btagged sample, normalised to fit results (a). Figure (b) shows the identical distribution from (a), but it is tagged via JFc. The same applies to Figure (c), where MV1 has been used.

60 7 b-Tagging

Table 7.1: Flavour fraction for different btagging algorithms.

flavour fraction	JF	JFc	MV1	pretag
			0.87	0.54
c quark	0.11	0.05		0.36
light quark	0.00	0.00	0.00	0.07

Table 7.2: Flavour fraction for different btagging algorithms at high cut values.

flavour fraction	JF	JFc	MV1	pretag
b quark c quark	1.00	0.99 0.01	0.91 0.09	$0.54 \\ 0.36$
light quark	0.00	0.00	0.00	0.07

Since the statistic in the selected sample is still high enough, it is feasible to investigate higher purity working points. To evaluate if more stringent cuts on the b-tagging weight variable are useful, their weight distributions must be investigated. Figure 7.6 shows the individual weight distributions of the tag-jet for all three taggers, after applying a cut on the respective working points defined above. In Figure 7.6(a) the JF weight distribution indicates, that at higher weights (> 6.0) virtually no charm-quark jet remains, while the the number of b-quark jets is still large. Figure 7.6(b) shows the same distribution, obtained with the JFc. At high weights of above 3.0 the b fraction approaches unity. Figure 7.6(c) illustrates the MV1 weight distribution of the tag-jet. In contrast to the previous two taggers, the c-quark contribution persists even in the highest bin, rendering its separation power inferior to the JF and the JFc b-taggers. The c-quark jets are peaking in the signal region. No cut can be applied to the MV1 weight distribution, which yields an absolutely pure b-flavoured sample.

In order to quantify the above made statements about the evolution of the b fraction with higher cut values, a new set of weights for each tagger is chosen:

• MV1: w > 0.98

• JF: w > 6.0

• JFc: w > 3.0

Figure 7.7 illustrates the impact on the secondary vertex mass distribution of the away-jet, for all three taggers at their new cut values. Table 7.2 summarises the flavour fraction at the increased cut values.

The calibration is conducted to support the single top-quark analysis, which is bound to the currently recommended MV1 b-tagger. Since a neural network is used in

the single top-quark analysis, it would benefit from a continuous calibration function. As seen in Figure 7.8, the weight distribution of the MV1 tagger provides an almost binary decision, thus rendering the additional information that can be obtained beyond a cut-based analysis, minimal. At this point the b-tagging calibration is deemed unfeasible and is discontinued.

This Section showed several indications, that the currently used MV1 b-tagger could impair the performance of single top-quark analyses. In the next section comparison studies are conducted to address that particular question.

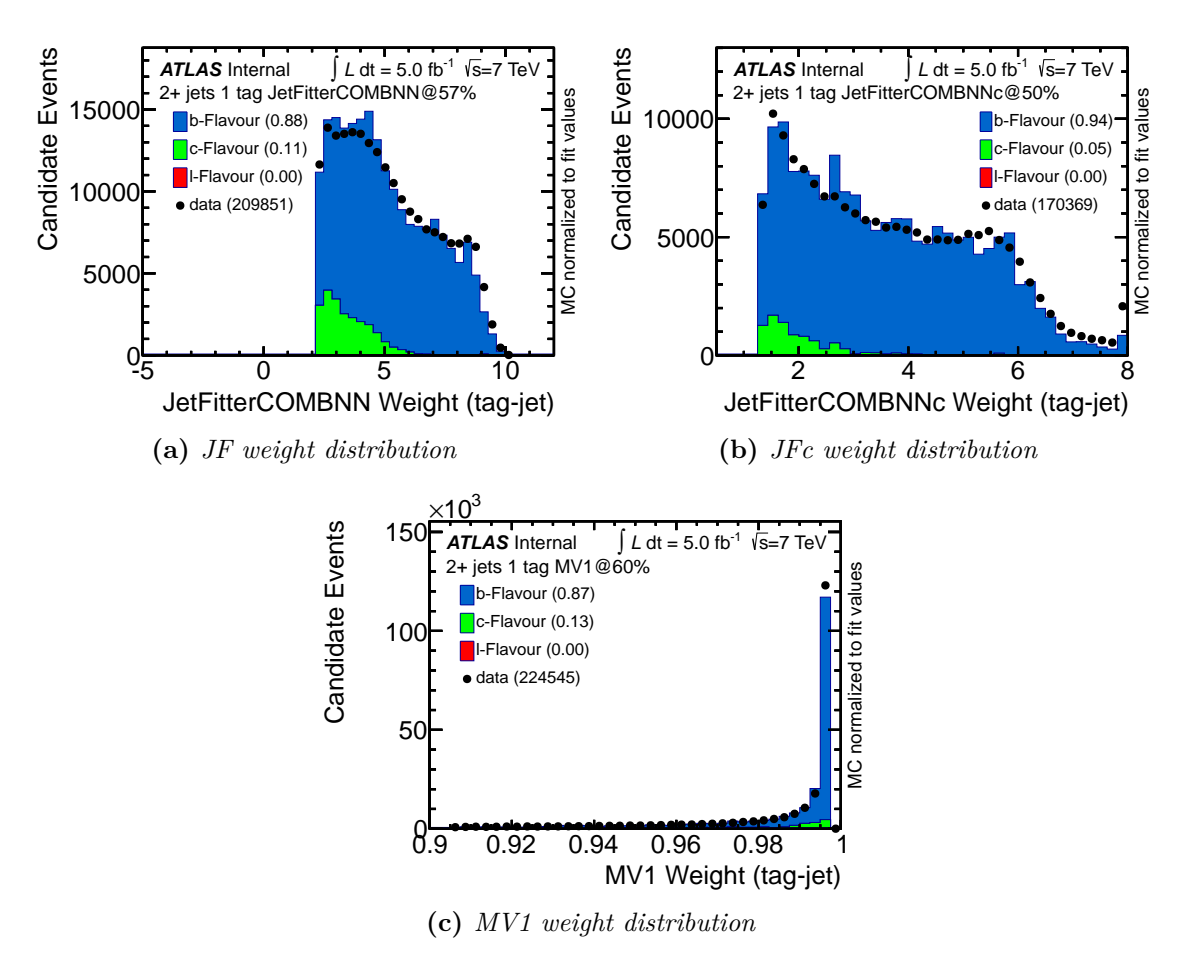


Figure 7.6: Stacked weight distributions of the tag-jet after each individual cut at the mentioned working points has been applied. All distributions are normalised to the fit values.

62 7 b-Tagging

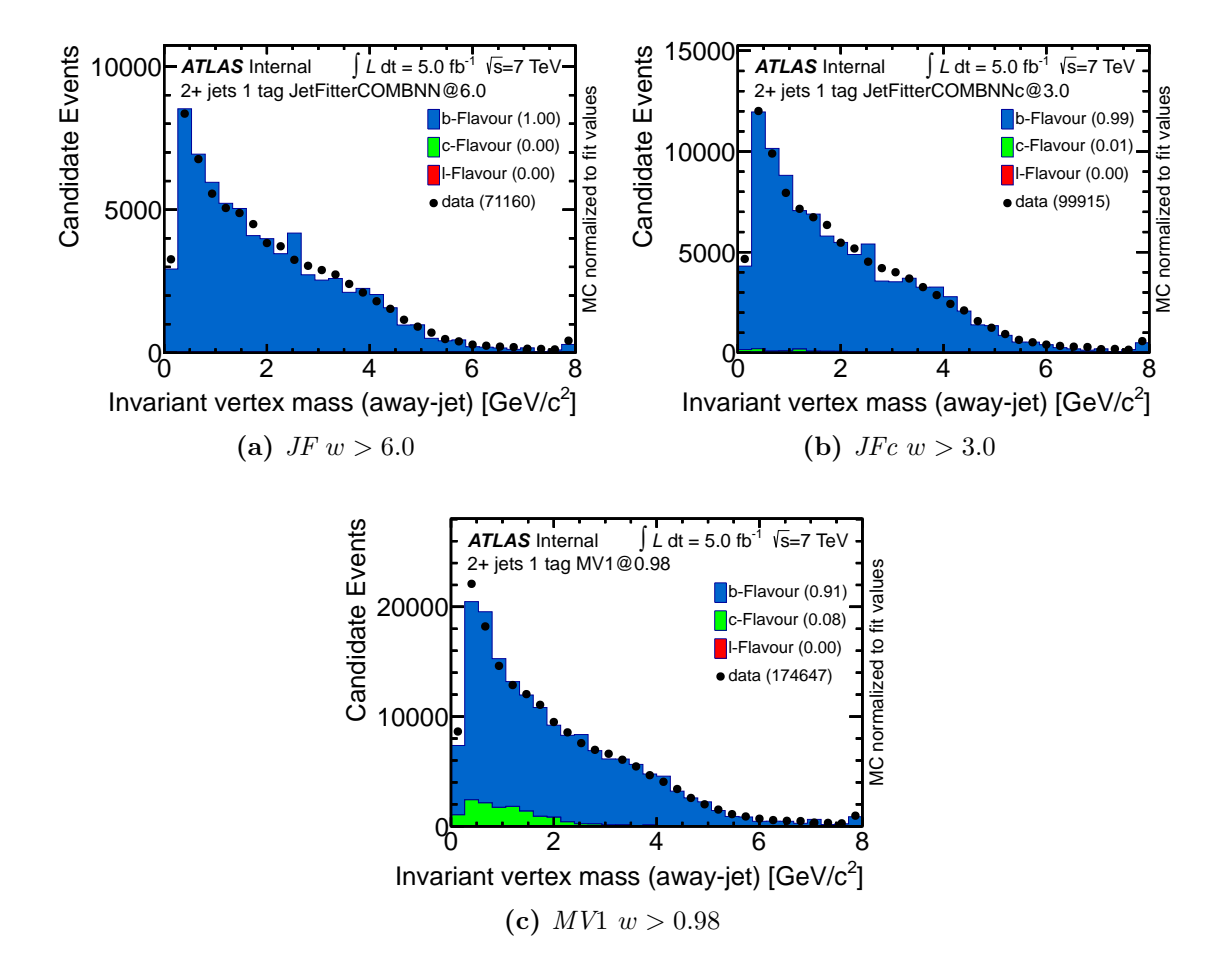


Figure 7.7: Secondary vertex mass distribution of the away-jet in the JF b-tagged sample, normalised to fit results (a). Figure (b) shows the identical distribution from (a), but it is tagged via JFc. The same applies to Figure (c), where MV1 has been used.

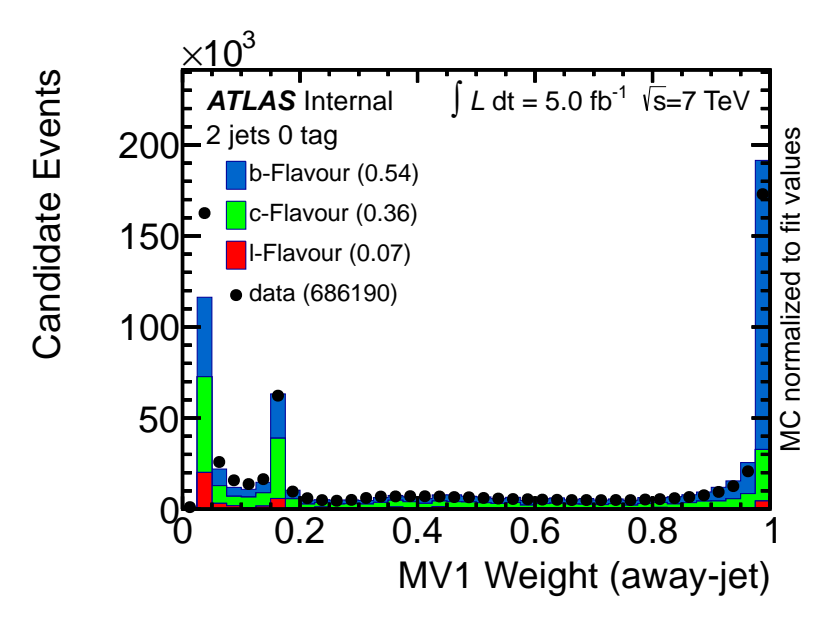


Figure 7.8: Weight distribution of the MV1 b-tagger of the pre-tagged sample. The distribution is peaking at high values and low values, but only a small separation between flavour components can be observed.

8 b-tagging Algorithms for Single Top-Quark Analyses

In single top-quark analyses, like in all top-quark analyses, a bottom-quark jet is a distinct feature. A good understanding of this key feature enables a better event reconstruction. In Section 8.2, a comparison study between three different b-tagging algorithms in single top-quark t-channel analyses is conducted. Section 8.3 introduces an approach to combine the JF and JFc and the resulting tagger is evaluated.

The last Section 8.4 is devoted to the evaluation of b-tagging uncertainties for two different b-tagging algorithms in the scope of single top-quark t-channel analyses.

8.1 Event Selection and Signature

In order to distinguish signal events from background events, requirements are defined which improve the fraction of signal events within all selected events. A so-called cut-based analysis consists of two classes of requirements, event requirements and object requirements. The first group are conditions that a whole event must satisfy, to be considered signal-like. The second group are conditions that an object within an event must satisfy, to be considered signal-like. The distinctiveness of the signal process is of vital importance to perform a cut-based analysis.

For single top-quark t-channel analyses only events in the so called leptop+jets channel are considered. Muons and electrons are accepted as the lepton which is stemming from the W-boson decay. Electron candidates are reconstructed offline using a cluster-based algorithm and are required to have $E_{\rm T} > 25$ GeV and $|\eta_{\rm cl}| < 2.47$, where $\eta_{\rm cl}$ denotes the pseudorapidity of the calorimeter cluster. Clusters falling in the calorimeter barrel-end-cap transition region, corresponding to $1.37 < |\eta_{\rm cl}| < 1.52$, are ignored.

Electrons must also be well isolated: the sum of the calorimeter transverse energy within a cone of radius $\Delta R = \sqrt{\Delta \eta^2 + \Delta \phi^2} = 0.2$ (excluding the cells associated with the electron) is required to be below a certain threshold that depends on the electron $E_{\rm T}$, the electron η and the number of reconstructed primary vertices and is

chosen such that the efficiency for real electrons to pass this isolation requirement is 90%. In addition, the $p_{\rm T}$ of all tracks within a cone of radius $\Delta R = 0.3$ around the electron direction, again excluding the track belonging to the electron, is also restricted to fall below an $E_{\rm T}$ -dependent threshold. The efficiency for this track-based isolation requirement is also 90% for real electrons.

Muon candidates are reconstructed by combining track segments found in the inner detector and in the muon spectrometer. Candidates are considered that have $p_{\rm T} > 25$ GeV and $|\eta| < 2.5$. Muon candidates are also required to be isolated. The sum of the calorimeter transverse energy within a cone of radius $\Delta R = 0.2$ is required to be below 4 GeV, while the $p_{\rm T}$ of all tracks within a cone of radius $\Delta R = 0.3$ must be below 2.5 GeV.

In addition, processes can contain a fake b-quark jet (multi-jet production). Since the multi-jet background is difficult to model precisely, we reduce its contribution through a requirement on the transverse mass of the lepton- $\rlap/E_{\rm T}$ system which resembles the transverse mass of the W boson for W+ jets events:

$$m_{\mathrm{T}}(W) = \sqrt{2p_{T}(\ell) \cancel{E}_{\mathrm{T}} \left[1 - \cos \Delta \phi \left(\ell, \cancel{E}_{\mathrm{T}}\right)\right]}$$
, with
$$m_{\mathrm{T}}(W) > 30 \text{ GeV}.$$

The W-boson decay also produces a neutrino which is detected as missing transverse momentum $\not\!\!E_T$. Since the $\not\!\!E_T$ in the event is originating from a W-boson decay, we define a minimum $\not\!\!E_T > 30$ GeV. In addition, two or three jets are required, completing the signal event signature. One of those jets originates from a b quark. Thus b-tagging requirements is imposed on one of the jets.

Particle jets are reconstructed using the anti- k_t algorithm [45] with a distance parameter of 0.4. The response of the calorimeter is corrected through a $p_{\rm T}$ - and η -dependent factor, which is derived from simulated events and validated with data.

Jets overlapping with selected electron candidates within $\Delta R < 0.2$ are removed, as in these cases the jet and the electron are very likely to correspond to the same physics object. Only jets having $p_{\rm T} > 25$ GeV and $|\eta| < 4.5$ are considered. Jets in the end-cap-forward calorimeter transition region, corresponding to $2.75 < |\eta| < 3.75$, must have a $p_{\rm T} > 50$ GeV. To reject jets from pile-up events, a quantity called jet-vertex fraction $\epsilon_{\rm jvf}$ is defined as the ratio of $\sum p_{\rm T}$ for all tracks within the jet that originate from the primary vertex associated to the hard-scattering collision to the $\sum p_{\rm T}$ of all tracks matched to the jet; and it is required that $|\epsilon_{jvf}| > 0.75$ for those jets which have associated tracks. Jets containing b-quarks are tagged in the region $|\eta| < 2.5$. The $E_{\rm T}$ is calculated using topological clusters and corrected for the presence of electrons, muons, and jets.

In the so called two-jet bin which contains events exactly two jets, the single top-quark t-channel acceptance is dominant. In the two-jet bin one jet is expected to be a b-quark jet which the other jet is a light-quark jet. The three-jet bin also contains a significant fraction of the single top-quark t-channel events, while in the four-jet bin the $t\bar{t}$ background becomes unfeasibly large. More details on the event selection, can be taken from Reference [48].

The selection criteria, which are applied to all events, allow for certain background processes to pass, so called irreducible background. Also various background processes can mimic signal events due to the false identification of selected objects. In general two different background types are present, processes which are too similar to the signal and the attempt to extract these processes, would decrease the resulting statistics. The significance of other background types arises from a much higher process cross section in relation to the signal cross section. Than even a small probability for a mis-identification will result in a non-negligible background contribution in the selected phase space.

In events containing exactly two jets from which one must be b-tagged, several background processes are relevant. W production with associated heavy-flavour quarks is the dominant background contribution. Figure 8.1 gives two example Feynman diagrams of the W+heavy flavour background production. Diagram 8.1(a) illustrates a W-boson production in association to a gluon splitting into a heavy-quark pair, while diagram 8.1(b) shows the W-boson production, plus an additional parton, in form of a gluon, as well as one c quark. The contribution of the $W+c(c\bar{c})$ processes arises from the probability of a b-tagger to misidentify a c-quark jet as a b quark jet, the so called mistag. A b-tagger with enhanced c-quark jet rejection capabilities could substantially reduce this particular background.

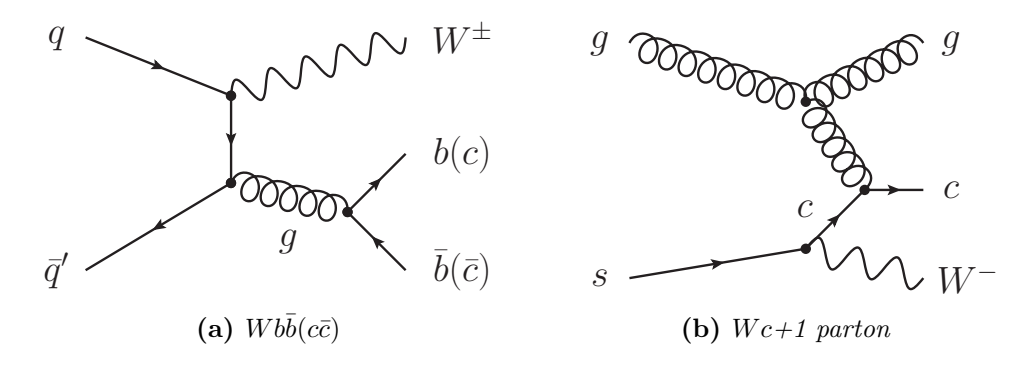


Figure 8.1: Examples of Feynman diagrams of W+heavy flavour background production: 8.1(a) shows the production of a W boson in association to a gluon splitting into a heavy-quark pair. 8.1(b) illustrates the production of a W boson in addition to a c quark and a gluon as an extra parton.

The top-quark pair production, illustrated in Figure 2.2, is another important

background for single top-quark t-channel production. The $t\bar{t}$ background is very persistent against cuts, since a top quark in the final state is similar to the signature of the signal. The diboson production, as well as the Z+jets production, is exemplarily depicted in Figure 8.2. Diagram 8.2(a) illustrates the diboson process, where WW, ZZ and WZ events can be produced. Figure 8.2(b) shows a diagram of Z+jets production, of which only the leptonic decay mode of the Z boson is considered.

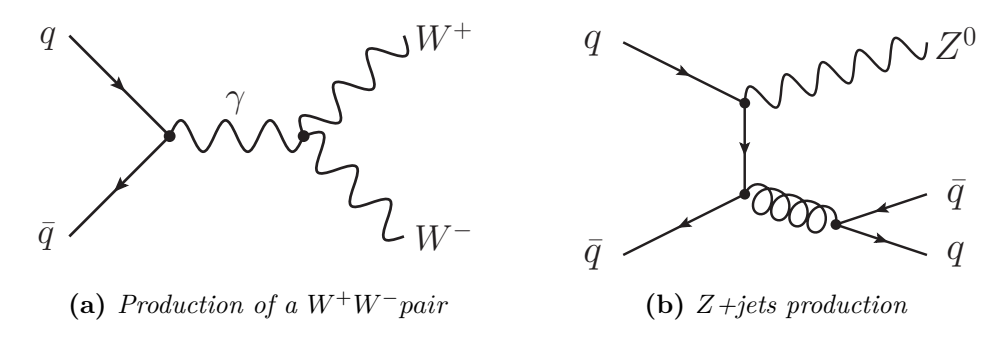


Figure 8.2: Example Feynman diagrams for the diboson and the Z+jets background production. ZZ, WW and WZ bosons can be produced in the final state of (a).

8.2 Comparison of b-tagging Algorithms in Single Top-Quark Analyses

In this section the performance of three b-tagging algorithms is compared. Single top-quark analyses rely strongly on the performance of the used b-tagger. For current analyses it is officially recommenced to use the MV1 b-tagger. In the previous section (7.3) indications have been found, that the MV1 b-tagger performs worse than the alternative JF b-tagger.

As described in Section 8.1, the dominant background contribution in single topquark analyses is W+jets production as well as the $t\bar{t}$ production. In particular the W+c jet process fraction forms the largest number of background events, as illustrated in Figure 8.3, it is therefore desirable to reduce this particular background. As shown in Section 7.3, the JF b-tagger and especially the JFc b-tagger provide an improved rejection capability for background processes with charm flavour jets, compared to the MV1 b-tagger. In Figure 8.3 the weight distribution of all three b-taggers is shown in the pre-tagged sample. The JF and JFc taggers display a decreasing fraction of W+c and W+light events at high weights, while these processes even peak at high weights in the MV1 weight distribution.

Figure 8.4 shows the weight distributions of all three taggers at the corresponding working points with the highest purity. The rejection behaviour of c-flavoured jet, that has been observed in Section 7.3, can be observed in Figure 8.4 as well. The JF and especially the JFc b-taggers are rejecting most of the charm background, while c-jets and light-flavoured jets peak within the highest bin of the MV1 b-tagger.

As a measure of comparison between multiple taggers, the Signal/Background (S/B) quantity is used. S/B is high if the sample contains mostly signal events compared to background events. The number of events that pass each individual cut are summarised in Table 8.1. At the bottom of the table the S/B quantity is calculated for all three taggers, as well as the S/B where only W+c(cc, light) is considered and the fraction of W+c(cc) events of all background MC events. In the last two columns the relative difference of both the JF and the JFc to the MV1 tagger are calculated. If the MV1 tagger at the working point with the highest purity is used, S/B is equal to 11.3%. A gain of 9% can be obtained by using the JF b-tagger instead. In comparison to the MV1 tagger, the JF provides a reduction of 21% of the W+c-jet background. By using the JFc tagger instead of the MV1 tagger, the S/B can be increased by 47%, as well as a 74% reduction of W+c-jet background.

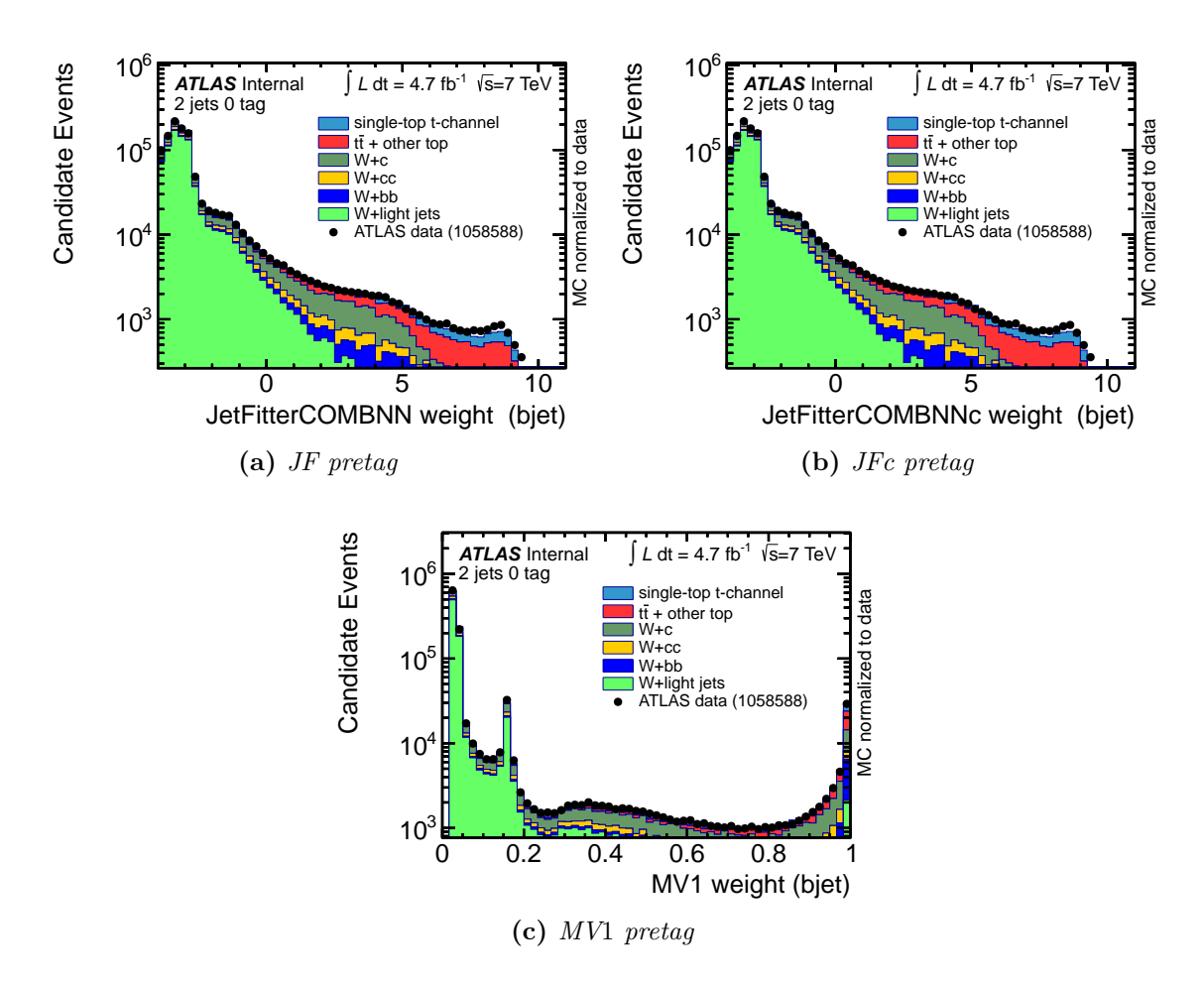


Figure 8.3: Weight distributions of all three b-taggers in the pre-tagged sample.

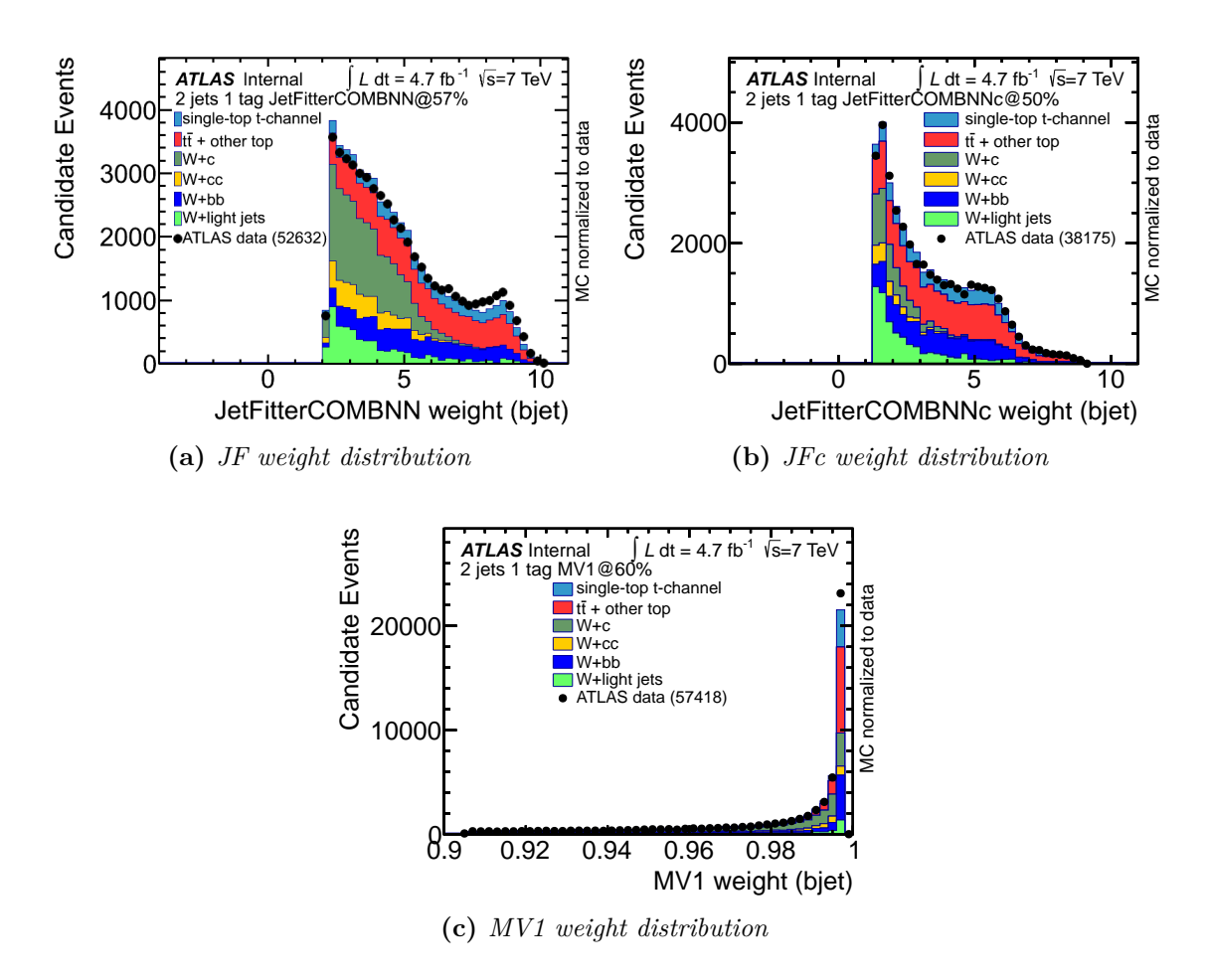


Figure 8.4: Weight distributions of the b-tagged jet after a cut at the mentioned working points has been applied. All distributions are normalised to data.

Table 8.1: MC composition of pre-tagged and tagged sample. At the bottom the S/B quantity for all three taggers are calculated, as well as the S/B where only W+c(cc, light) is considered and the fraction of W+c(cc) events of all background MC events. In the last two columns the relative difference of both the JF and the JFc to the MV1 tagger are calculated.

Process	pre-tag	MV1@60%	m JF@57%	m JFc@50%	Δ_{rel}	Δ_{rel}
	1				(MV1,JF)	(MV1,JFc)
					(111 / 1,01)	(111 (1,01 0)
single-top t -channel	9618	4693	4488	4391	-4%	-6%
ttbar + other top	23966	11383	10998	10766	-3%	-5%
W + bb jets	21052	6360	6124	6011	-4%	-5%
W + cc jets	53054	4237	3303	1212	-22%	-71%
W + c jets	121292	14496	11389	3377	-21%	-77%
W+light jets	607912	5220	4757	5153	-9%	-1%
S/B	1.2%	11.3%	12.3%	16.6%	+9%	+47%
S/B (W + (c, cc, light))	1.2%	19.6%	23.1%	45.1%	+18%	+130%
Bkg fraction c, cc	26.7%	81.6%	67.2%	20.9%	-18%	-74%
0	,0	0=10,0	7 0	0.070	1 -0,0	, 0

8.3 b-tagging Optimisation

In Section 8.2 the improved performance of the JetFitter based b-taggers compared to the MV1 has been established. In Table 8.1 the relative differences in W + c jets and W + light jets rejection are given. Compared to the JF, the JFc provides an improved W + c jets rejection and vice versa. As discussed in Section 7.2, both derivatives of the JetFitterCOMB b-tagger, are likelihood ratios of three probabilities. Each tagger uses either p_u and p_b , or p_b and p_c likelihoods. It has been stated, that every b-tagger which is build on the likelihood ratio formalism, can be combined by adding the individual tagger weights.

A combination of both the JF and the JFc taggers, potentially provide an enhanced rejection of charm and light flavour jets background compared to each individual tagger. The weight of each individual tagger has been defined as:

$$w_{\rm JF} \equiv \log\left(\frac{p_b}{p_u}\right)$$
 (8.1)

$$w_{\rm JFc} \equiv \log\left(\frac{p_b}{p_c}\right).$$
 (8.2)

A linear combination of both taggers can be parameterised as:

$$w_{JF\alpha} \equiv \log\left(\frac{pb}{\alpha \cdot pu + (1-\alpha) \cdot pc}\right),$$
 (8.3)

where α is between 0 and 1. The resulting b-tagger is called JF α .

The event yield of single top-quark t-channel analyses is sampled in intervals of $\Delta \alpha = 0.05$ between 0 and 1. S/B is evaluated from a histogram for each bin. Each bin of a S/B histogram is filled with the ratio of integral of the corresponding bins in a signal- and background histogram. The integral is the sum of the current bin i to the last bin I.

$$S/B_i = \frac{\sum_{i=0}^{I} S(i)}{\sum_{i=0}^{I} B(i)}$$
 (8.4)

In this case S/B is not calculated to the last bin for i, but to a previously obtained limit i_{max} . The limit is given by the desired number of signal events and is thereby fixing the tagging efficiency. The desired number of signal events of the JF @57% is obtained from Table 8.1 ($N_{min}^{signal} = 4488$). Bin i_{max} satisfies the relation:

$$N_{min}^{signal} = \sum_{i_{max}}^{I} S(i) \tag{8.5}$$

and has therefore the property, that all higher bins contain N_{min}^{signal} events. The maximum S/B quantity is evaluated for every value of α . Figure 8.5 shows the S/B values as a function of α . The maximum S/B value is 0.165 at $\alpha=0.45$. The fluctuation of the S/B values is due to the binning of the respective signal and background histograms. Because of the fluctuations a value for $\alpha=0.5$ is chosen for further evaluation. The corresponding cut weight is obtained via the previously calculated S/B histogram for $\alpha=0.5$. The cut weight is therefore w=1.75 which is equal to the x-value of the bin i_{max} .

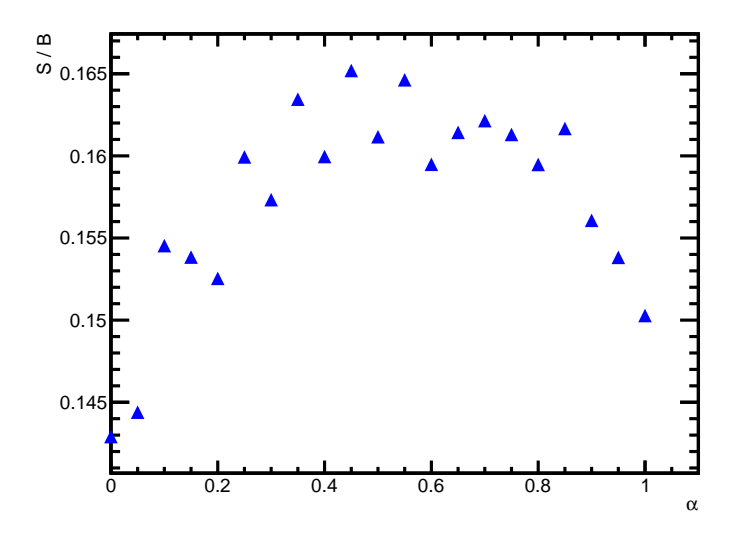


Figure 8.5: S/B values as a function of α . The maximum is S/B = 0.165 at $\alpha = 0.45$.

Table 8.2: MC composition of pre-tagged and tagged sample. At the bottom the S/B quantity for all three taggers are calculated, as well as the S/B where only W+c(cc, light) is considered and the fraction of W+c(cc) events of all background MC events. In the last two columns the relative difference of both the JF (JF) and the JFc (JFc) to the $JF\alpha$ ($JF\alpha$) tagger are calculated.

Process	pre-tag	JF@57%	JFc@50%	${ m JF} \alpha @ 1.75$	$\begin{array}{ c c } \Delta_{rel} \\ (JF, JF\alpha) \end{array}$	$\begin{array}{c} \Delta_{rel} \\ (\mathrm{JFc}, \mathrm{JF}\alpha) \end{array}$
single-top t-channel	9618	4488	4391	3924	-13%	-11%
$t\bar{t}$ + other top	23966	10998	10766	10007	-9%	-7%
W + bb jets	21052	6124	6011	5309	-13%	-12%
W + cc jets	53054	3303	1212	1149	-65%	-5%
W + c jets	121292	11389	3377	3277	-71%	-3%
W + light jets	607912	4757	5153	3563	-25%	-31%
S/B	1.2%	12.3%	16.6%	16.8%	+37%	+2%
S/B (W + (c, cc, light))	1.2%	23.1%	45.1%	49.1%	+113%	+9%
Bkg fraction c, cc	26.7%	67.2%	20.9%	23.4%	-65%	+12%

Table 8.2 contains the MC composition of the pre-tagged sample, as well as for the JF, the JFc and the JF α . At the bottom the S/B quantity for all three taggers are calculated, as well as the S/B where only W+c(cc, light) is considered and the fraction of W+c(cc) events of all background MC events. In the last two columns the relative difference of both the JF (JF) and the JFc (JFc) to the JF α (JF α) tagger are calculated. If the JF α with $\alpha=0.5$ is used with a cut weight of w=1.75, the resulting S/B=16.8. In relation to the JF and the JFc taggers the JF α provides an improved S/B value of 37 and 2 percent, but the signal yield decreases 13 and 11 percent respectively. Since the significant loss in signal efficiency is not compensated with an substantial increase of the S/B value, the combination is deemed less effective than the JFc tagger.

An alternative approach of combining both the JF and the JFc b-taggers, is to apply them consecutively. Figure 8.6 illustrates the two dimensional weight distribution, after the taggers at the individually working points of highest purity have been applied. In Table 8.3 the contributions of the used MC samples are given. An alternative cut value for the JFc tagger is chosen for better comparison, since the new cut-value yields as much signal events, as the tagger combination. Compared to the JFc tagger at a cut of w=2.0, the combination yields a 86% decline in W+c jets rejection and a 18% decrease in W+ light jets rejection. The S/B quantity is reduced by 10% compared to the JFc.

In conclusion both combinations do not yield improved performance with respect to the JFc tagger. The deviance to the results of the optimisation, is stemming from the fact that, in the scope of the determination of the value α , only one jet per

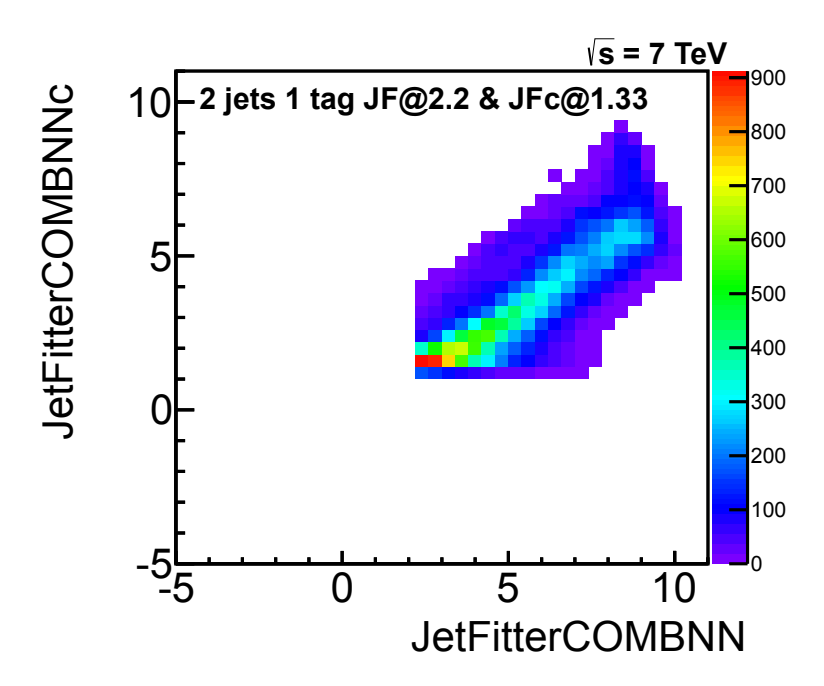


Figure 8.6: Two dimensional weight distribution of the JF and the JFc taggers for the tagged sample.

event is considered. The jet which is selected has the lowest pseudorapidity of both jets within an event. If the b-tagging is applied, both jets are evaluated, thereby enhancing the probability of a background jet within an event. For the same reason, the number of signal events is reduced compared to the pre-fixed value N_{min}^{signal} , when the b-tagging is applied.

Table 8.3: MC composition of the tagged sample. At the bottom the S/B quantity for all three taggers are calculated, as well as the S/B where only W+c(cc, light) is considered and the fraction of W+c(cc) events of all background MC events. In the last two columns the relative difference of both the JF and the JFc to the combination of both taggers are calculated.

Process	$\rm JFc@50\%$	${\rm JFc@2.0}$	$\rm JF@57\%$	Δ_{rel}	Δ_{rel}
			$+\mathrm{JFc}@50\%$	(JFc50,JF+JFc)	(JFc2.0,JF+JFc)
single-top t-channel	4391	3723	3715	-15%	0%
$t\bar{t}$ + other top	10766	9107	8964	-17%	-2%
W + bb jets	6011	4979	4947	-18%	-1%
W + cc jets	1212	517	955	-21%	+85%
W + c jets	3377	1492	2769	-18%	+86%
W + light jets	5153	2627	3112	-40%	+18%
$\overline{S/B}$	16.6%	19.9%	17.9%	+8%	-10%
S/B (W + (c, cc, light))	45.1%	80.3%	54.3%	+21%	-32%
Bkg fraction c, cc	20.9%	12.0%	21.9%	+5%	+82%

8.4 Evaluation of Systematic Uncertainties

Section 8.2 yielded that single top-quark analyses would benefit from using the JF and especially the JFc b-taggers instead of the currently recommended MV1. In order to evaluate the performance of the JFc tagger, the impact on the systematic uncertainty of the analysis has to be considered. Within the JFc two existing working points, at 50% and 55%, are compared.

In case of single top analyses several systematic uncertainties have to be considered, yet in the scope of this thesis, only the uncertainty associated to the b-tagging are compared. A b-tagging calibration yields scale factors, in order to account for differences in rate, between measured data and the MC model. The jet $p_{\rm T}$ - and η -dependent scale factors have uncertainties which range from 8% to 16% and 23% to 45%, respectively [48].

As stated in [48], the b-tagging scale-factor systematic uncertainty is one of the dominant uncertainties in this particular analysis. Since the use of the JFc tagger would significantly increase the S/B quantity, an slight elevation in the systematic b-tagging uncertainty can be deemed acceptable.

The statistical analysis to obtain the magnitude of the systematical uncertainties, is based on a frequentist method. The output of the used neural network provides template shape distributions. These template distributions and the acceptance of signal and background processes are taken into account. Pseudo experiments are generated according to the systematic shifts. The entire set of pseudo data has been created with random variations of systematic influences.

For this analysis 150 000 pseudo experiments are created. Table 8.4 contains the b-tagging scale-factor uncertainty, subdivided in top quark and top antiquark processes. The up and down fluctuation as well as the calculated bias are presented for the MV1@60%, JetFitterCOMBNNc@55% and JetFitterCOMBNNc@50% b-taggers. Since all up and down fluctuations are individually symmetric, the values are summarised in Table 8.5. This Table also contains the relative differences between the MV1@60% and the JetFitterCOMBNNc@55% and JetFitterCOMBNNc@50% b-taggers. In case of the JFc@55%, the systematic b-tagging scale-factor uncertainty is reduced by 5.0% and 0.5% for the top quark and top antiquark processes respectively, compared to MV1@60%. The comparison between MV1@60% and JetFitterCOMBNNc@50% yields -3.4% for the top antiquark process and +2.9% for the top quark process.

In conclusion, the JetFitterCOMBNNc@55% yields a lower b-tagging scale-factor uncertainty for both, top quark and top antiquark processes. In case of the JetFitterCOMBNNc@50%, the b-tagging scale-factor uncertainty for both, top quark and top antiquark processes, is approximately the same as those of the MV1@60% b-tagger.

 ${\sf Table~8.4:}~\textit{b-tagging~scale-factor~uncertainty}.$

Process	N	IV1@60%
t-channel top antiquark t -channel top quark	up [%] 8.789 7.463	down [%] -8.789 -7.463
	JetFitter	CombNNc@55%
t-channel top antiquark t -channel top quark	up [%] 8.349 7.429	down [%] -8.349 -7.429
	JetFitter	CombNNc@50%
t-channel top antiquark t -channel top quark	up [%] 8.487 7.679	down [%] -8.487 -7.679

Table 8.5: Comparison of b-tagging scale-factor uncertainties.

	WV1	JFc55	JFc50	Δ_{rel} (MV1,JFc55)	Δ_{rel} (MV1,JFc50)
t-channel top antiquark	8.789	8.349	8.487	-5.0%	-3.4%
t-channel top quark	7.463	7.429	7.679	-0.5%	+2.9%

9 Conclusion

The presented studies use collision data recorded with the ATLAS detector in 2011. The LHC was operated at $\sqrt{s} = 7$ TeV center-of-mass energy in this time period.

The single top-quark can be produced with charged electroweak interaction and can occur in three different production modes. At the LHC the single top-quark t-channel is the dominant production mechanism. In order to understand the modeling of the single top-quark t-channel events provided by MC generators, the first part of this thesis, studies of the kinematic properties of the single top-quark t-channel have been conducted. These kinematic properties of the final state particles of the single top-quark t-channel have been compared between MC event generators and with NLO calculations using the MCFM framework. The direct comparison between AcerMC and POWHEG, yielded a very good agreement in most of the studied observables. The light-quark distribution is the only noteworthy difference between the generators, which can be explained by the ambiguous definition of the light quark in the presence of final state radiation. The comparison of either AcerMC and POWHEG to MCFM had shown that the objects calculated at NLO with MCFM are not fully understood and can be studied further.

A Standard Model top-quark decays into a W boson and a b quark with nearly 100% probability, therefore the identification capability of a b-quark jet is important for most physics processes involving top quarks. b-tagging, is used to efficiently reduce high cross-section backgrounds which does not involve the production of a b-quark. The performance of single top-quark analyses depends on the understanding of b-tagging. Different b-tagging algorithms are available exploiting the characteristics of the b-quark jet. All b-tagging algorithms need to be calibrated, to account for modeling differences between the simulated events and the collision data. These calibrations are performed for defined working points corresponding to a certain tagging efficiency, and provide scaling factors. A b-tagging calibration for single top-quark t-channel analyses have been conducted to obtain a continuous scaling function for use in neural networks, but could not be completed.

For these studies a dijet MC sample was purified to contain mostly bb events, using a tag-and-probe method. In the course of the preparation of the b-tagging calibration it is necessary to obtain a pure b-quark jet sample. A series of three b-taggers have been tested at their individually working points providing maximum

82 9 Conclusion

purity. The studies on the purification of the dijet MC sample indicated, that the MV1 b-tagging algorithm provides inferior c-quark jet rejection capabilities compared to the JetFitterCOMBNNc b-tagger. The MV1 b-tagger displayed a problematic background behaviour, in terms of the planned application in single top-quark t-channel analyses using Neural Network techniques.

Since the single top-quark t-channel analyses have been officially recommended to use the MV1 b-tagger at the time the calibration was conducted, it was not feasible to continue. The MV1 weight distribution could have been used for the calibration, but at first a more viable b-tagger for which a calibration could be conducted is searched. The indications that the use of the MV1 b-tagger entails a inferior c-quark jet rejection lead to a further investigation of the influence on the performance of single top-quark t-channel analyses. In those particular analyses, the c-quark jet rejection plays a crucial role, since the W boson production in addition with one or two c-quark jets are major background processes, due to the possible mis-identification of the c-quark jet as a b-quark jet.

The comparison of b-tagging algorithms is performed using single top-quark t-channel MC samples, as well as a set of background MC samples, containing top-quark associated background and W+jets processes with b-, c- and light-jets in the final state. The JetFitterCOMBNN and the JetFitterCOMBNNc have yielded superior S/B ratios compared to the MV1 tagger. A sub-optimal performance of the MV1 b-tagging algorithm in single top-quark t-channel analyses have been observed in this thesis. An attempt to combine the JetFitterCOMBNN and JetFitterCOMBNNc taggers did not yield improved performance with respect to the JetFitterCOMBNNc tagger.

The best choice of the presented taggers for single top-quark t-channel analyses is the JetFitterCOMBNNc at 50% b-tagging efficiency, with can increase the S/B by 47% from 11.3% to 16.6%, compared to MV1 at 60% b-tagging efficiency. It is important to estimate the influence on the uncertainty of single top-quark t-channel analysis prior to any recommendations. The b-tagging scale-factor uncertainty is evaluated for single top-quark t-channel analyses, by using a frequentist approach. The recommended MV1 b-tagger is compared to the JetFitterCOMBNNc b-tagger. A comparison between MV1 at 60% b-tagging efficiency and JetFitterCOMBNNc at 50% b-tagging efficiency yields -3.4% for the top antiquark process and +2.9% for the top quark process.

In the meantime the JetFitterCOMBNNc is officially recognised as a b-tagger that can be used in single top-quark t-channel analyses instead of the MV1 b-tagger. The results obtained in this thesis supported the official decision towards approving the use of this b-tagger.

List of Figures

2.1	Feynman diagram of e^+ , e^- annihilation	(
2.2	Dominant leading-order top-quark pair production modes at the LHC.	7
2.3	Leading-order single top-quark production modes	7
2.4	Examples for next-to-leading-order single top-quark t-channel correc-	
		8
2.5	Parton distribution function	L]
3.1	A schematic view of the LHC layout	14
3.2	Delivered LHC luminosity	15
3.3	ATLAS detector	17
3.4		16
3.5	ATLAS Inner Detector	2(
3.6	· ·	22
3.7	ATLAS Muon System	
3.8	Trigger system	25
4.1	Basic MC generator structure	28
4.2	Detector Simulation	34
5.1	Final state t-channel signature	36
5.2	Examples for real and virtual next-to-leading-order corrections 3	3
6.1	Vertex reconstruction efficiency and fake vertex probability	49
7.1	Impact Parameter	5.
7.2	Signed IP distribution	5
7.3	MV1 weight distribution	5(
7.4		58
7.5		59
7.6	0 0 1	3.
7.7		32
7.8	MV1 pre-tag weight distribution	33
8.1	W+heavy flavour background	
8.2	Z+jets background	36
8.3	Pre-tagged away-jet secondary vertex mass distribution	7(

84 List of Figures

8.4	Weight distribution of all three algorithms in the tagged sample	71
8.6	Two dimensional weight distribution of the JF and the JFc taggers	
	for the tagged sample	76

List of Tables

2.12.22.3	Fermions of the Standard Model	4
3.1 3.2	LHC Parameters	
4.1 4.2 4.3	Pythia dijet MC sample, subdivided by jet multiplicities Top quark MC samples, for single top quark production and $t\bar{t}$ Background MC samples for single top-quark analyses	32
5.1	Ren. and Fac. scale for MCFM	40
7.1 7.2	Flavour fraction for different b tagging algorithms Flavour fraction for different b tagging algorithms at high cut values	
8.1 8.2 8.3 8.4	MC composition. MV1 vs. JF and JFc	75 77
8.5	Comparison of b-tagging scale-factor uncertainties	79

- [1] Tevatron Electroweak Working Group, for the CDF and D0 Collaborations. Combination of CDF and D0 results on the mass of the top quark using up to 5.8 fb-1 of data. 2011. 16 pages, 2 figures. URL: http://inspirehep.net/record/920234/export/hx, arXiv:1107.5255.
- [2] F. Abe et al. Observation of top quark production in $\bar{p}p$ collisions. Phys. Rev. Lett., 74:2626-2631, 1995. arXiv:hep-ex/9503002, doi:10.1103/PhysRevLett.74.2626.
- [3] S. Abachi et al. Observation of the top quark. *Phys. Rev. Lett.*, 74:2632–2637, 1995. arXiv:hep-ex/9503003, doi:10.1103/PhysRevLett.74.2632.
- [4] F. Reif. Fundamentals of Statistical and Thermal Physics. McGraw Hill, Tokyo, 1965.
- [5] R. P. Feynman. Space-Time Approach to Quantum Electrodynamics. *Phys. Rev.*, 76:769–789, Sep 1949. URL: http://link.aps.org/doi/10.1103/PhysRev.76.769, doi:10.1103/PhysRev.76.769.
- [6] J. Beringer et al. Review of Particle Physics. *Journal of Physics G*, D86, 2012. URL: http://pdg.lbl.gov.
- [7] Steven Weinberg. Conceptual Foundations of the Unified Theory of Weak and Electromagnetic Interactions. pages 215–223, 1991.
- [8] A. Quadt. Top quark physics at hadron colliders. European Physical Journal C, 48:835–1000, December 2006. doi:10.1140/epjc/s2006-02631-6.
- [9] Nikolaos Kidonakis. Next-to-next-to-leading-order collinear and soft gluon corrections for t-channel single top quark production. Phys.Rev.D83:091503, 2011. arXiv:arXiv:1103.2792, doi:10.1103/PhysRevD.83.091503.
- [10] Nikolaos Kidonakis. NNLL resummation for s-channel single top quark production. Phys.Rev.D81:054028, 2010. arXiv:arXiv:1001.5034, doi:10.1103/PhysRevD.81.054028.
- [11] Nikolaos Kidonakis. Two-loop soft anomalous dimensions for single top quark associated production with a *W* or *H*-. Phys.Rev.D82:054018, 2010. arXiv: arXiv:1005.4451, doi:10.1103/PhysRevD.82.054018.

[12] Rikkert Frederix, Emanuele Re, and Paolo Torrielli. Single-top t-channel hadroproduction in the four-flavour scheme with POWHEG and aMC@NLO, 2012. arXiv:1207.5391.

- [13] Rikkert Frederix. Top quark phenomenology, 2010. arXiv:arXiv:1009.6199.
- [14] Hung-Liang Lai, Marco Guzzi, Joey Huston, Zhao Li, Pavel M. Nadolsky, Jon Pumplin, and C. P. Yuan. New parton distributions for collider physics. Phys.Rev.D82:074024, 2010. arXiv:arXiv:1007.2241, doi:10.1103/PhysRevD.82.074024.
- [15] Evans and Bryant. LHC Machine. JINST, 3:S08001, 2008. doi:10.1088/1748-0221/3/08/S08001.
- [16] Daniel Fournier. Performance of the LHC, ATLAS and CMS in 2011. Technical report, 2012. arXiv:1201.4681, doi:10.1051/epjconf/20122801003.
- [17] The ATLAS Collaboration, 2012. URL: http://www.atlas.ch/.
- [18] Luminosity Determination in pp Collisions at $\sqrt{s}=7$ TeV using the ATLAS Detector in 2011. Technical Report ATLAS-CONF-2011-116, CERN, Geneva, Aug 2011.
- [19] G. Aad et al. The ATLAS Experiment at the CERN Large Hadron Collider. JINST, page 437, 2008.
- [20] Estimating Track Momentum Resolution in Minimum Bias Events using Simulation and K_s in $\sqrt{s} = 900$ GeV collision data. Technical Report ATLAS-CONF-2010-009, CERN, Geneva, Jun 2010.
- [21] M. Aharrouche and ATLAS Electromagnetic Barrel Calorimeter Collaboration. Energy Linearity and Resolution of the ATLAS Electromagnetic Barrel Calorimeter in an Electron Test-Beam. Nucl.Instrum.Meth.A568:601-623,2006, 2006. arXiv:arXiv:physics/0608012, doi:10.1016/j.nima.2006.07.053.
- [22] Muon reconstruction efficiency in reprocessed 2010 lhc proton-proton collision data recorded with the atlas detector. Technical Report ATLAS-CONF-2011-063, CERN, Geneva, Apr 2011.
- [23] The ATLAS Collaboration. Performance of the ATLAS Trigger System in 2010. Eur.Phys.J.C 72 (2012) 1849, 2011. arXiv:arXiv:1110.1530, doi: 10.1140/epjc/s10052-011-1849-1.
- [24] R Hauser. The ATLAS Trigger System. Jun 2003.
- [25] M.A. Dobbs et al. Les Houches Guidebook to Monte Carlo Generators for Hadron Collider Physics, 2004. arXiv:arXiv:math/0403045.
- [26] Stefano Frixione and Bryan R. Webber. Matching NLO QCD computations and parton shower simulations. *JHEP*, 0206:029, 2002. arXiv:hep-ph/0204244.

[27] G. Corcella, I.G. Knowles, G. Marchesini, S. Moretti, K. Odagiri, et al. HERWIG 6: An Event generator for hadron emission reactions with interfering gluons (including supersymmetric processes). *JHEP*, 0101:010, 2001. arXiv:hep-ph/ 0011363.

- [28] Torbjorn Sjostrand, Stephen Mrenna, and Peter Z. Skands. A Brief Introduction to PYTHIA 8.1. *Comput.Phys.Commun.*, 178:852-867, 2008. arXiv:0710.3820, doi:10.1016/j.cpc.2008.01.036.
- [29] A. Bialas and M. Gyulassy. Lund model and an outside-inside aspect of the inside-outside cascade. *Nuclear Physics B*, 291(0):793 812, 1987. URL: http://www.sciencedirect.com/science/article/pii/0550321387904962, doi: 10.1016/0550-3213(87)90496-2.
- [30] Borut Paul Kersevan and Elzbieta Richter-Was. The Monte Carlo event generator AcerMC version 2.0 with interfaces to PYTHIA 6.2 and HERWIG 6.5. 2004. arXiv:hep-ph/0405247.
- [31] The powheg box homepage, 2012. URL: http://powhegbox.mib.infn.it.
- [32] Michelangelo L. Mangano, Mauro Moretti, Fulvio Piccinini, Roberto Pittau, and Antonio D. Polosa. ALPGEN, a generator for hard multiparton processes in hadronic collisions. *JHEP*, 0307:001, 2003. arXiv:hep-ph/0206293.
- [33] S. Agostinelli et al. GEANT4: A Simulation toolkit. *Nucl.Instrum.Meth.*, A506:250–303, 2003. doi:10.1016/S0168-9002(03)01368-8.
- [34] M.A.G. Aivazis, John C. Collins, Fredrick I. Olness, and Wu-Ki Tung. Leptoproduction of heavy quarks. 2. A Unified QCD formulation of charged and neutral current processes from fixed target to collider energies. *Phys.Rev.*, D50:3102–3118, 1994. arXiv:hep-ph/9312319, doi:10.1103/PhysRevD.50.3102.
- [35] M.A.G. Aivazis, Frederick I. Olness, and Wu-Ki Tung. Leptoproduction of heavy quarks. 1. General formalism and kinematics of charged current and neutral current production processes. *Phys.Rev.*, D50:3085–3101, 1994. arXiv: hep-ph/9312318, doi:10.1103/PhysRevD.50.3085.
- [36] John M Campbell and R. K. Ellis. Mcfm for the tevatron and the lhc. Nucl.Phys.Proc.Suppl.205-206:10-15,2010, 2010. arXiv:arXiv:1007.3492, doi: 10.1016/j.nuclphysbps.2010.08.011.
- [37] John Campbell, R. K. Ellis, and Francesco Tramontano. Single top production and decay at next-to-leading order. Phys.Rev.D70:094012,2004, 2004. arXiv: arXiv:hep-ph/0408158, doi:10.1103/PhysRevD.70.094012.
- [38] T Cornelissen, M Elsing, I Gavrilenko, W Liebig, E Moyse, and A Salzburger. The new ATLAS track reconstruction (NEWT). *Journal of Physics: Conference Series*, 119(3):032014, 2008. URL: http://stacks.iop.org/1742-6596/119/i=3/a=032014.

[39] Rudolph Emil Kalman. A New Approach to Linear Filtering and Prediction Problems. *Transactions of the ASME-Journal of Basic Engineering*, 82(Series D):35–45, 1960.

- [40] Performance of primary vertex reconstruction in proton-proton collisions at \sqrt{s} =7 TeV in the ATLAS experiment. Technical Report ATLAS-CONF-2010-069, CERN, Geneva, Jul 2010.
- [41] Performance of the ATLAS Inner Detector Track and Vertex Reconstruction in the High Pile-Up LHC Environment. Technical Report ATLAS-CONF-2012-042, CERN, Geneva, Mar 2012.
- [42] Electron and photon reconstruction and identification in atlas: expected performance at high energy and results at 900 gev. Technical Report ATLAS-CONF-2010-005, CERN, Geneva, Jun 2010.
- [43] ATLAS Collaboration. Electron performance measurements with the atlas detector using the 2010 lhc proton-proton collision data. Eur. Phys. J. C72 (2012) 1909, 2011. arXiv:arXiv:1110.3174, doi:10.1140/epjc/s10052-012-1909-1.
- [44] Muon reconstruction performance. Technical Report ATLAS-CONF-2010-064, CERN, Geneva, Jul 2010.
- [45] Matteo Cacciari, Gavin P. Salam, and Gregory Soyez. The anti- kt jet clustering algorithm. *Journal of High Energy Physics*, 2008(04):063, 2008. URL: http://stacks.iop.org/1126-6708/2008/i=04/a=063.
- [46] ATLAS, The collaboration. Measuring the b-tag efficiency in a top-pair sample with $4.7fb^{-1}$ of data from the ATLAS detector. Technical Report ATLAS-CONF-2012-097, CERN, Geneva, Jul 2012.
- [47] F Filthaut and C Weiser. The Identification of b-Jets with the ATLAS Detector. Technical Report ATL-COM-PHYS-2012-824, CERN, Geneva, Jun 2012.
- [48] K Becker, D Hirschbuehl, P Sturm, and W Wagner. Measurement of the t-channel single top-quark and top-antiquark production cross-sections and their ratio in pp collisions at $\sqrt{s}=7$ TeV. Technical Report ATLAS-COM-CONF-2012-028, CERN, Geneva, Feb 2012.
- [49] Georg Sartisohn and W Wagner. Higgs Boson Search in the $H \to WW^{(*)} \to \ell\nu\ell\nu$ Channel using Neural Networks with the ATLAS Detector at 7 TeV. oai:cds.cern.ch:1456081. PhD thesis, Wuppertal U., Mar 2012. Presented 08 May 2012.

Selbstständigkeitserklärung / Eidesstattliche Erklärung

Der Verfasser erklärt an Eides statt, dass er die vorliegende Arbeit selbständig, ohne fremde Hilfe und ohne Benutzung anderer als die angegebenen Hilfsmittel angefertigt hat. Die aus fremden Quellen (einschliesslich elektronischer Quellen) direkt oder indirekt übernommenen Gedanken sind ausnahmslos als solche kenntlich gemacht. Die Arbeit ist in gleicher oder ähnlicher Form oder auszugsweise im Rahmen einer anderen Prüfung noch nicht vorgelegt worden.

Wuppertal, 14.09.2012